



HAL
open science

Numerical investigations on the dynamic behavior of a 2-DOF airfoil in the transitional Re number regime based on fully coupled simulations relying on an eddy-resolving technique

Guillaume de Nayer, Michael Breuer, Jens Nikolas Wood

► **To cite this version:**

Guillaume de Nayer, Michael Breuer, Jens Nikolas Wood. Numerical investigations on the dynamic behavior of a 2-DOF airfoil in the transitional Re number regime based on fully coupled simulations relying on an eddy-resolving technique. *International Journal of Heat and Fluid Flow*, 2020, 85, pp.108631. 10.1016/j.ijheatfluidflow.2020.108631 . hal-02910909

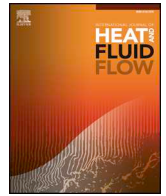
HAL Id: hal-02910909

<https://hal.science/hal-02910909>

Submitted on 3 Aug 2020

HAL is a multi-disciplinary open access archive for the deposit and dissemination of scientific research documents, whether they are published or not. The documents may come from teaching and research institutions in France or abroad, or from public or private research centers.

L'archive ouverte pluridisciplinaire **HAL**, est destinée au dépôt et à la diffusion de documents scientifiques de niveau recherche, publiés ou non, émanant des établissements d'enseignement et de recherche français ou étrangers, des laboratoires publics ou privés.



Numerical investigations on the dynamic behavior of a 2-DOF airfoil in the transitional Re number regime based on fully coupled simulations relying on an eddy-resolving technique

G. De Nayer, M. Breuer*, J.N. Wood

Professur für Strömungsmechanik, Helmut-Schmidt-Universität Hamburg, D-22043 Hamburg, Germany

ARTICLE INFO

Keywords:

Fluid–structure interaction
2-DOF aeroelastic oscillations
Limit-cycle oscillation
Airfoil flutter
Large-eddy simulation
Partitioned approach

ABSTRACT

The paper is the numerical counterpart of the experimental investigation on the fluid–structure interaction (FSI) of a wing with two degrees of freedom (DOF), i.e., pitch and heave. Wood et al. (2020) has provided the experimental basis by studying the flutter stability of an elastically mounted straight wing (NACA 0012 airfoil) in a wind tunnel considering the transitional Reynolds number regime. Three different configurations with varying distances between the fixed elastic axis and the variable center of gravity were considered. Additional free-oscillation tests in still air were carried out in order to make the mechanical properties of the setup available for the simulations. The present contribution describes the numerical methodology applied consisting of a partitioned coupled solver combining eddy-resolving large-eddy simulations on the fluid side with a solver for the governing equations of the translation and rotation of the rigid wing. In order to prove the parameters provided by the experiment and to determine the pure material damping coefficients not available from the measurements, simulations of 1-DOF free-oscillation tests in still air are carried out and analyzed. For validation purposes the corresponding 2-DOF free-oscillation tests in still air are assessed and a good agreement with the experimental data is achieved. Finally, the wing exposed to a constant free-stream of varying strength is analyzed leading to the characterization of complex instantaneous FSI phenomena such as limit-cycle oscillations and flutter. Under full utilization of the supplementary measurements the predictions are evaluated in detail. Contrary to the experiments the simulations provide the entire fluid data and unique data for the translatory and rotatory movement allowing to investigate the causes of the observed phenomena. Both limit-cycle oscillations and flutter can be reproduced by the coupled FSI predictions.

1. Introduction

Complementary experimental and numerical investigations are of fundamental importance in order to investigate multi-physics problems. Combining the advantages of both methods leads to a better understanding of complex physical processes such as fluid–structure interactions (FSI). The present study is concerned with measurements and numerical predictions of the oscillation behavior of an elastically mounted airfoil in the transitional Reynolds number regime. Typical technical examples that fall into this Re range are unmanned air vehicles including Micro Air Vehicles (MAV) (Shyy et al., 1999; Mueller, 2001; Lian et al., 2003). Here, specific flow phenomena such as laminar separation bubbles (LSB) and transition occur in combination with oscillations of the structure rendering this a very challenging case (Breuer, 2018) especially for numerical simulations.

For the transitional Reynolds number regime considered a literature review on experimental and numerical investigations of oscillating airfoils was presented in the study by Wood et al. (2020) and will not be repeated here. The setup experimentally investigated in Wood et al. (2020) is based on a rigid NACA 0012 airfoil elastically mounted in a wind tunnel exhibiting two degrees of freedom, i.e., heave and pitch. Based on this setup, three configurations with the same elastic axis and a variable center of gravity were taken into account in order to fully expose the dynamic response of the oscillating system and to discuss its stability: In *case I* the position of the center of gravity (c.o.g.) approximately coincides with the location of the elastic axis (e.a.). In *case II* the c.o.g. is positioned towards the leading edge and in *case III* it is shifted close to the trailing edge. Based on one degree of freedom (1-DOF) free-oscillation tests in still air, the relevant parameters of each case (mass, mass moment of inertia, spring stiffness and total damping)

* Corresponding author.

E-mail address: breuer@hsu-hh.de (M. Breuer).

<https://doi.org/10.1016/j.ijheatfluidflow.2020.108631>

Received 23 March 2020; Received in revised form 25 May 2020; Accepted 26 May 2020

0142-727X/ © 2020 The Authors. Published by Elsevier Inc. This is an open access article under the CC BY license (<http://creativecommons.org/licenses/by/4.0/>).

accuracy (Breuer et al., 2012). Since the Reynolds number of the present case (based on the chord of the airfoil) varies in the range $9.66 \times 10^3 \leq \text{Re} \leq 3.60 \times 10^4$, the flow is in the transitional regime. Therefore, turbulence is taken into account by the large-eddy simulation (LES) technique (Breuer, 2002), i.e., the large scales of the turbulent flow field are resolved directly, whereas the small scales are modeled by a subgrid-scale (SGS) model. In the simulations presented below the standard Smagorinsky SGS model (Smagorinsky, 1963) with a well established constant $C_S = 0.1$ and van-Driest damping near solid walls is applied. In order to justify this choice, additional simulations based on the dynamic variant of the Smagorinsky model suggested by Germano et al. (1991) and Lilly (1992) were carried out. Only marginal differences between the predictions with the fixed and the dynamic version of the Smagorinsky model were detected. The reason for this minor influence of the subgrid-scale model is attributed to the low Reynolds numbers considered, where turbulence partially plays a role solely in the wake of the airfoil.

For FSI applications the semi-implicit predictor-corrector scheme was extended to a partitioned coupling scheme which considers the specific needs of LES and FSI, i.e., high temporal resolution and strong stability at high fluid-to-structure density ratios (Breuer et al., 2012). In this context the temporally varying domain is taken into account by the Arbitrary Lagrangian-Eulerian formulation. In the present FSI case the oscillating airfoil will undergo significant translational movements and particularly large rotations. For instance, the flutter instability in case III is simulated up to a heave of $\Delta z_{\max}/c > \pm 0.5$ and a pitch of $\Delta \alpha_{\max} > \pm 60^\circ$. Therefore, in order to adapt the fluid mesh to the new position of the airfoil, the hybrid adaption method recently proposed by Sen et al. (2017) and especially developed for FSI problems relying on LES is applied. It is based on a combination of an inverse distance weighting (IDW) interpolation for the block boundaries of the block-structured grid and a three-dimensional transfinite interpolation (TFI) for the inner mesh. Taking the moving nodes of the FSI interface into account, this hybrid technique delivers a deformed grid of high quality as will be shown below: The orthogonality and aspect ratio of the control volumes near the movable airfoil remain nearly unchanged, which is essential for LES. Note that the present case of the flow around a rigid object could also be simulated based on a grid which is moved and/or rotated as a whole. Nevertheless, this option was not taken into account here, since this case also serves as a further validation study for the developed FSI-LES simulation methodology targeting flexible structures.

In the last decade this solver was intensively enhanced, tested and validated relying on complementary experimental and numerical pure CFD or FSI applications (Breuer et al., 2012; Kalmbach and Breuer, 2013; De Nayer et al., 2014; De Nayer and Breuer, 2014; Wood et al., 2016; De Nayer et al., 2018; De Nayer et al., 2018; Apostolatos et al., 2019).

3.2. Computational structure dynamics (CSD)

In the present FSI application the airfoil is considered as a rigid body (see Fig. 1), i.e., it does not suffer any deformations. Therefore, the response of the structure to the fluid occurs only in form of displacements of the entire structure. In order to solve the dynamics of the airfoil experiencing fluid forces and moments, a solver describing the movement of the rigid body is applied. For this purpose, Newton's second law is solved in the Cartesian basis $R_0 = (x, y, z)$ for the translational $\vec{X} = (X_1, X_2, X_3)$ and rotational $\vec{\varphi} = (\varphi_1, \varphi_2, \varphi_3)$ motions, respectively. Leroyer and Visonneau (2005) wrote these equations in the form of a coupled system for the general case considering a moving deformable body. The equations for the translational motion are written at the center of gravity denoted c.o.g. or G by Wood et al. (2020), whereas the equations for the rotation are written at the elastic axis (e.a. or E). Based on the notations used in Wood et al. (2020) the

coupled system reads:

$$\begin{bmatrix} m_w & 0 & 0 & 0 & z_{EG} m_w & -y_{EG} m_w \\ 0 & m_w & 0 & -z_{EG} m_w & 0 & x_{EG} m_w \\ 0 & 0 & m_w & y_{EG} m_w & -x_{EG} m_w & 0 \\ 0 & -z_{EG} m_w & y_{EG} m_w & I_{11}^E & I_{12}^E & I_{13}^E \\ z_{EG} m_w & 0 & -x_{EG} m_w & I_{21}^E & I_{22}^E & I_{23}^E \\ -y_{EG} m_w & x_{EG} m_w & 0 & I_{31}^E & I_{32}^E & I_{33}^E \end{bmatrix} \begin{bmatrix} \dot{X}_1 \\ \dot{X}_2 \\ \dot{X}_3 \\ \dot{\varphi}_1 \\ \dot{\varphi}_2 \\ \dot{\varphi}_3 \end{bmatrix} + \begin{bmatrix} b_{t,1} & 0 & 0 & 0 & 0 & 0 \\ 0 & b_{t,2} & 0 & 0 & 0 & 0 \\ 0 & 0 & b_{t,3} & 0 & 0 & 0 \\ 0 & 0 & 0 & b_{r,1} & 0 & 0 \\ 0 & 0 & 0 & 0 & b_{r,2} & 0 \\ 0 & 0 & 0 & 0 & 0 & b_{r,3} \end{bmatrix} \begin{bmatrix} \dot{X}_1 \\ \dot{X}_2 \\ \dot{X}_3 \\ \dot{\varphi}_1 \\ \dot{\varphi}_2 \\ \dot{\varphi}_3 \end{bmatrix} + \begin{bmatrix} k_{t,1} & 0 & 0 & 0 & 0 & 0 \\ 0 & k_{t,2} & 0 & 0 & 0 & 0 \\ 0 & 0 & k_{t,3} & 0 & 0 & 0 \\ 0 & 0 & 0 & k_{r,1} & 0 & 0 \\ 0 & 0 & 0 & 0 & k_{r,2} & 0 \\ 0 & 0 & 0 & 0 & 0 & k_{r,3} \end{bmatrix} \begin{bmatrix} X_1 \\ X_2 \\ X_3 \\ \varphi_1 \\ \varphi_2 \\ \varphi_3 \end{bmatrix} = \begin{bmatrix} F_{CFD,1} - S_{R,1} \\ F_{CFD,2} - S_{R,2} \\ F_{CFD,3} - S_{R,3} \\ M_{CFD,1} - S_{I,1} - S_{M,1} \\ M_{CFD,2} - S_{I,2} - S_{M,2} \\ M_{CFD,3} - S_{I,3} - S_{M,3} \end{bmatrix}, \quad (1)$$

with the inertial source term:

$$\vec{S}_I = \begin{bmatrix} S_{I,1} \\ S_{I,2} \\ S_{I,3} \end{bmatrix} = \int_{V(t)} \rho_s (\vec{EP} \cdot \vec{\varphi}) (\vec{EP} \times \vec{\varphi}) dV \quad (2)$$

$$= \begin{bmatrix} -\varphi_1 \varphi_3 I_{12}^E + \varphi_1 \varphi_2 I_{13}^E - (\varphi_3^2 - \varphi_2^2) I_{23}^E + \varphi_2 \varphi_3 (I_{33}^E - I_{22}^E) \\ -\varphi_1 \varphi_2 I_{23}^E + \varphi_2 \varphi_3 I_{12}^E - (\varphi_1^2 - \varphi_3^2) I_{13}^E + \varphi_1 \varphi_3 (I_{11}^E - I_{33}^E) \\ -\varphi_2 \varphi_3 I_{13}^E + \varphi_1 \varphi_3 I_{23}^E - (\varphi_2^2 - \varphi_1^2) I_{12}^E + \varphi_1 \varphi_2 (I_{22}^E - I_{11}^E) \end{bmatrix},$$

and the source terms induced by a body deformation or a rigid rotation:

$$\vec{S}_R = m_w [\underbrace{\vec{a}(G, R_1) + 2\vec{\varphi} \times \vec{v}(G, R_1)}_{**} + \vec{\varphi} \times (\vec{\varphi} \times \vec{EG})], \quad (3)$$

$$\vec{S}_M = \underbrace{\int_{V(t)} \rho_s \vec{EP} \times \vec{a}(P, R_1) dV}_{**} + 2 \underbrace{\int_{V(t)} \rho_s (\vec{v}(P, R_1) \cdot \vec{EP}) \vec{\varphi} dV}_{**} - 2 \underbrace{\int_{V(t)} \rho_s (\vec{EP} \cdot \vec{\varphi}) \vec{v}(P, R_1) dV}_{**}. \quad (4)$$

m_w and I_{ij}^E are the mass and the mass moment of inertia regarding the elastic axis E . The triplet (x_{EG}, y_{EG}, z_{EG}) contains the components of the vector from the elastic axis to the center of gravity G . $b_{t,i}$ and $b_{r,i}$ are the material damping coefficients for the translational and rotational motion. $k_{t,i}$ and $k_{r,i}$ represent the translational and rotational stiffness. F_{CFD} describes the fluid forces and M_{CFD} denotes the moments regarding the elastic axis E . ρ_s is the density of the structure. $\vec{v}(P, R_1)$ and $\vec{a}(P, R_1)$ represent the velocity and the acceleration vectors of a material point P of the airfoil in R_1 , which is a local Cartesian coordinate system (CCS) attached to the airfoil on the elastic axis. V is the structural volume considered.

The coupled system of Leroyer and Visonneau (2005) is now simplified for the current problem. A rigid airfoil is assumed, whose local CCS (R_1) is fixed on the elastic axis. Neither the c.o.g. G nor the material point P change their position with reference to the body-fixed CCS R_1 , when the rigid body is deflected. Therefore, the velocity vector \vec{v} and the acceleration vector \vec{a} in Eqs. (3) and (4) are zero and the terms

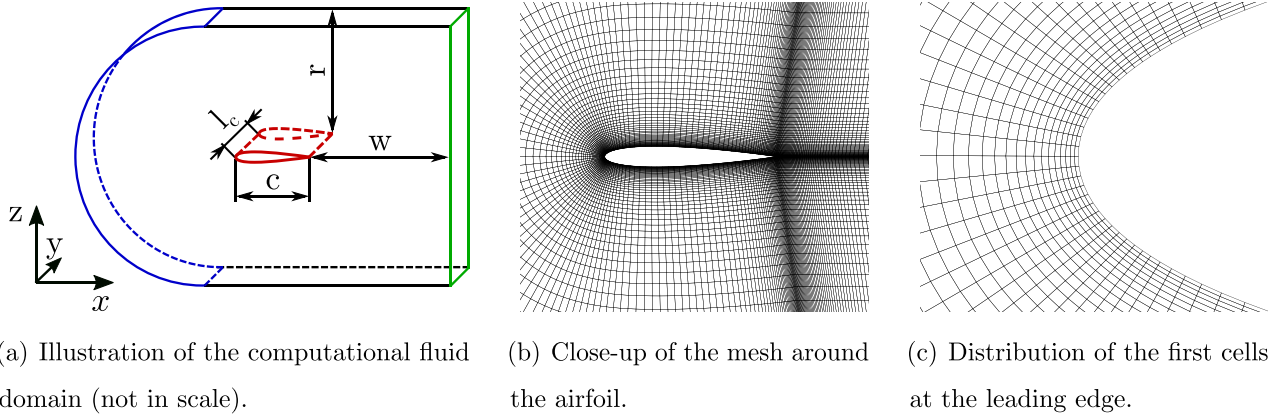


Fig. 2. CFD setup.

tagged with ** vanish. Moreover, due to its perpendicular axes, the non-diagonal moments of inertia vanish. Consequently, the terms in Eq. (2) marked with * are zero. Moreover, the setup has only 2-DOF, i.e., translation in the X_3 -direction and rotation around the X_2 -axis. Hence φ_1 and φ_3 are irrelevant and the inertial source term S_f vanishes completely. Introducing the notations $X_3 = z$, $\varphi_2 = \alpha$, $b_{i,3} = b_h$, $k_{i,3} = k_h$ and $I_{22}^E = I_\alpha^E$, the coupled system is simplified as follow:

$$\begin{aligned} m_w \ddot{z} + b_h \dot{z} + k_h z - \underbrace{x_{EG} m_w}_{***} \ddot{\alpha} &= F_{CFD,3} - S_{R,3}, \\ I_\alpha^E \ddot{\alpha} + b_\alpha \dot{\alpha} + k_\alpha \alpha - \underbrace{x_{EG} m_w}_{***} \ddot{z} &= M_{CFD,2}. \end{aligned} \quad (5)$$

The term *** is the so-called “static moment” often used in the literature but somehow misleading. In the present case it is the product of the mass m_w and the horizontal distance of the elastic axis E and the center of gravity G . In case that E coincides with G , the static moment disappears.

It is interesting to remark that this coupled system slightly differs from the classic system typically used for 2-DOF flutter investigations provided for example by Fung (2008): The translational equation of motion in vertical direction of a two-degrees-of-freedom airfoil section includes the additional term $S_{R,3}$ not appearing in Fung’s equations. In the present case, the term $S_{R,3}$ reads:

$$S_{R,3} = -m_w \dot{\alpha}^2 z_{EG}(t). \quad (6)$$

A possible explanation why this term was neglected in Fung (2008) and others is the fact that the vertical distance z_{EG} between E and G remains small for small angles of rotation. Nevertheless, in the present study the full system including $S_{R,3}$ is taken into account for the sake of completeness and correctness.

In order to avoid singularities during the computation of the rotation, the Euler angles are replaced by *quaternions* as used in Leroyer and Vissonneau (2005).

Note that in the present partitioned approach the time-step size is the same for the fluid and structure solvers. To get the solution of the motion at the new time-step $n + 1$, the coupled system in Eq. (5) is solved sequentially, since the time-step used by LES is very small. The terms $S \ddot{\alpha}$ and $S \ddot{z}$ are moved to the right-hand side and taken from the previous time-step n :

$$\begin{aligned} m_w \ddot{z}^{n+1} + b_h \dot{z}^{n+1} + k_h z^{n+1} &= F_{CFD,3}^{n+1} + x_{EG}^n m_w \ddot{\alpha}^n + z_{EG}^n m_w (\dot{\alpha}^n)^2, \\ I_\alpha^E \ddot{\alpha}^{n+1} + b_\alpha \dot{\alpha}^{n+1} + k_\alpha \alpha^{n+1} &= M_{CFD,2}^{n+1} + x_{EG}^n m_w \ddot{z}^n. \end{aligned} \quad (7)$$

The temporal discretization of the system of Eqs. (7) is implemented by using the *standard Newmark* method of second-order accuracy in time (Newmark, 1959) (Newmark parameters set to $\beta = 0.25$ and $\gamma = 0.5$).

3.3. Coupling procedure

Since the present numerical methodology relies on a standard partitioned approach (Breuer et al., 2012), the fluid forces and moments acting on the rigid body have to be transferred to the solver describing the movement of the rigid body. The fluid forces computed at the center of each cell face of the FSI interface are composed of the fluid pressure and the shear forces on the wall element. The resulting fluid force acting on the airfoil F_{CFD} and the corresponding moment M_{CFD} are transferred to the structure solver. Note that M_{CFD} is computed with reference to the elastic axis E . In the other direction, from the structure solver to the fluid solver, the structural displacement of the surface of the airfoil representing the FSI interface obtained by the superposition of translation and rotation around E is directly imposed at each fluid mesh nodes of the FSI interface. These displacements at the FSI interface between fluid and structure are the starting point of the hybrid grid adaptation technique transferring the movement of the interface to the inner CFD grid as explained above.

As previously mentioned the coupling scheme is standard, i.e., one or several FSI sub-iterations can be afforded, leading to a loose or strong FSI coupling, respectively. Since in the current application the ratio of the structure density to the fluid density is larger than 100, the added-mass effect (i.e., the additional inertia added to a moving body undergoing a relative velocity in a fluid) is negligible (Causin et al., 2005; Farhat et al., 2006). A loose coupling FSI scheme is sufficient and delivers quasi exact results (error below 0.2% on the extrema) in comparison to the results obtained by a strong coupling FSI scheme. The latter works without any underrelaxation of the forces/moments or the displacement, and applies a first-order estimation of the displacement at the beginning of each time-step. Since the loose coupling scheme saves a huge amount of CPU-time, it is preferred here.

4. Numerical setup of the system

4.1. CFD

Starting with the CFD setup, the computational domain for the fluid illustrated in Fig. 2a is characterized by the symmetric NACA 0012 airfoil exhibiting a chord length $c = 0.1$ m located at its center. The inlet as well as outlet are highlighted in blue and green, respectively. At the inlet a constant free-stream velocity U_∞ is assumed, which is sufficient here since the experimentally determined turbulence intensity is low Tu (Tu < 0.5%) (Wood et al., 2020). At the outlet a convective outflow boundary condition is prescribed with the convection velocity set to U_∞ . Symmetry boundary conditions are applied at the top and bottom, respectively. Furthermore, in spanwise direction periodic boundary conditions are applied. This choice and the associated specification of the extent of the flow domain is justified by previous investigations of

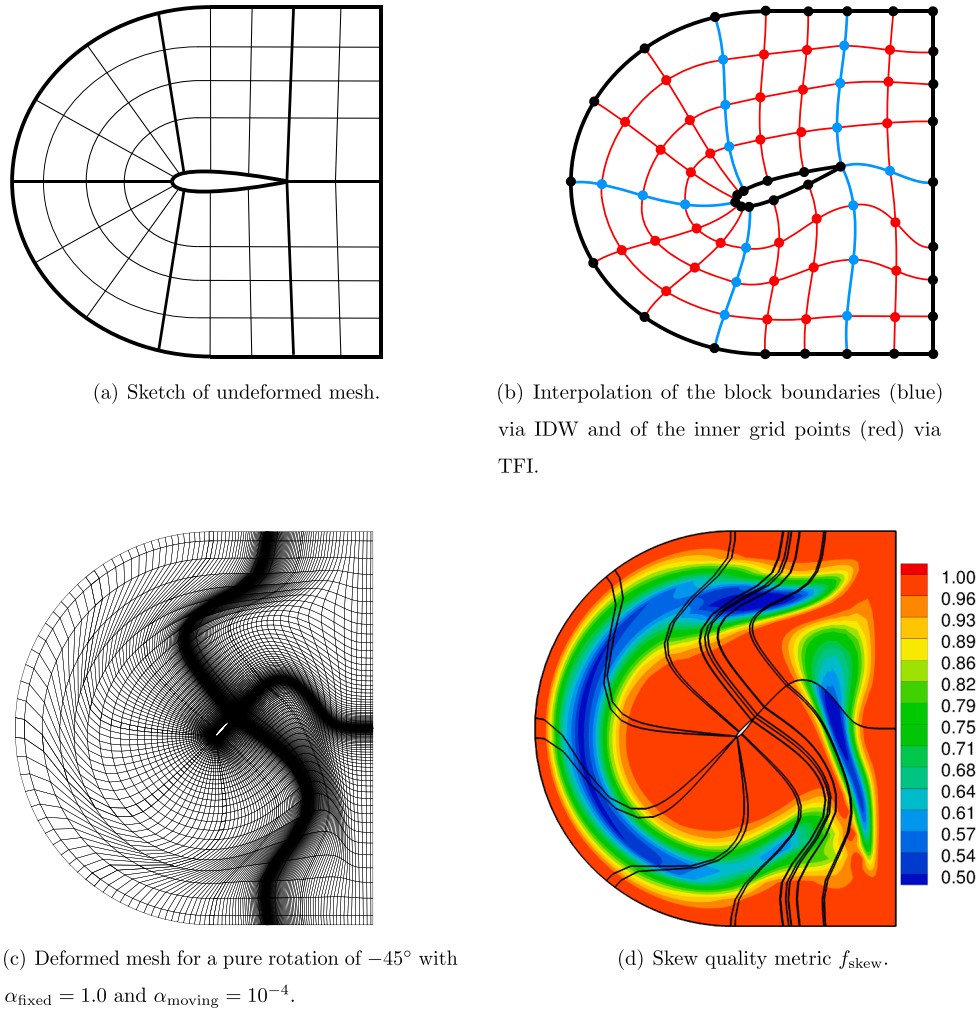


Fig. 3. Illustration of the hybrid IDW-TFI mesh adaption (Sen et al., 2017) for the present computational domain. In the vicinity of the airfoil f_{skew} is close to the optimum.

similar flow cases, c.f. Breuer (2018) and the references cited therein. Following the work of Almutari (2011) the wake length is specified as $w = 5c$, the semi-cylinder's radius is $r = 7.2c$ and the spanwise length is $l_c = 0.25c$.

The C-type mesh used in the simulations is shown in Fig. 2(b)–(c). It consists of 16 blocks with a total of 1,394,400 control volumes (CVs) and 1,507,188 nodes. 60 CVs are equidistantly distributed in spanwise direction. The distance between the first cell center and the wall in wall-normal direction is about 6.1×10^{-5} m and the stretching factor of the geometrical series applied in wall-normal direction is $q_s = 1.09$. With this setup the dimensionless wall distance at the smallest Reynolds number of $Re = 9.66 \times 10^3$ is smaller than one. It increases continuously with increasing Reynolds number. Since the dimensionless wall distance remains in the range of $0 \leq y^+ \leq 5$ at the Reynolds numbers considered, the viscous sublayer can be resolved and thus no-slip conditions are used.

As mentioned before the mesh is adapted by the hybrid IDW-TFI remeshing technique. An illustration of the method is presented in Fig. 3. The block boundaries (blue lines in Fig. 3b) are adjusted by the IDW method, whereas the inner grid points of each block (red lines) are adapted by the highly efficient TFI algorithm. In order to control the deformation of the grid, one set of parameters is required: A kind of stiffness for the grid deformation near the fixed outer boundary and the moving inner surface of the airfoil (α_{fixed} and α_{moving}) (Sen et al., 2017). Here, α_{fixed} is set to 1 and α_{moving} to 10^{-4} . A deformed mesh for the extreme case of a rotation by 45 degrees is exemplary depicted in

Fig. 3c with its associated skew quality metric (Fig. 3d) defined in Knupp (2003). It is obvious that the deformation of the grid is pushed away from the rigid structure and that the mesh near the moving boundaries translates and rotates as a block with the airfoil. Values of f_{skew} close to unity denote a very high orthogonality of the grid. Thus, the high grid quality regarding the grid point distribution and the orthogonality is maintained in the direct vicinity and the intermediate region around the airfoil. Note that the movement of the airfoil encountered during the investigations on airfoil oscillations are typically much more moderate. Hence, the example should solely demonstrate the capabilities of the grid adaption technique applied.

4.2. CSD

Wood et al. (2020) investigated three different configurations for the present setup:

- *Case I:* G approximately coincides with E , implying $m_w x_{EG} \approx 0$ and $S_{R,3}^I \approx 0$. Moreover, the two equations of motion (7) are uncoupled;
- *Case II:* G is located upstream of E , leading to a negative static moment $m_w x_{EG} < 0$ and $S_{R,3}^{II} \neq 0$;
- *Case III:* G is placed downstream of E , generating a positive static moment $m_w x_{EG} > 0$ and $S_{R,3}^{III} \neq 0$.

In order to correctly describe the dynamics of the present elastically mounted airfoil, the parameters m_w , b_h , k_h , I_α^E , b_α and k_α of the system

Table 2
Main parameters of all three configurations of the experimental setup (Wood et al., 2020).

Parameter	Symbol	Unit	Case I	Case II	Case III
Distance between c.o.g. and e.a.	x_{EG}/c	–	≈ 0	– 0.022	+ 0.059
Mass moment of inertia based on f_{α}^{1-DOF}	I_{α}^E	kg m ²	1.399×10^{-4}	1.73×10^{-4}	1.73×10^{-4}
Mass of dynamic system	m_w	kg	0.33521	0.33521	0.33521
Bending stiffness	k_h	N/m	698	698	698
Torsional stiffness	k_{α}	Nm/rad	0.3832	0.3832	0.3832
Total translational damping in still air	$b_h^{1-DOF,tot}$	Ns/m	9.72×10^{-2}	8.57×10^{-2}	16.28×10^{-2}
Total rotational damping in still air	$b_{\alpha}^{1-DOF,tot}$	Nm/s	3.70×10^{-5}	3.94×10^{-5}	4.54×10^{-5}
Total translational damping ratio in still air	$D_h^{1-DOF,tot}$	–	3.18×10^{-3}	2.80×10^{-3}	5.32×10^{-3}
Total rotational damping ratio in still air	$D_{\alpha}^{1-DOF,tot}$	–	2.53×10^{-3}	2.42×10^{-3}	2.79×10^{-3}

Table 3
Numerically predicted material damping ratios for all three cases.

Parameter	Symbol	Unit	Value
Translational material damping ratio	D_h^{1-DOF}	–	2.30×10^{-3}
Rotational material damping ratio	D_{α}^{1-DOF}	–	1.15×10^{-3}

(7) have to be set. Furthermore, the position of the center of gravity G has to be determined. Table 2 summarizes these parameters determined by Wood et al. (2020) based on their experimental data.

It is important to note that the damping coefficients $b_h^{1-DOF,tot}$ and

$b_{\alpha}^{1-DOF,tot}$ and the associated damping ratios $D_h^{1-DOF,tot}$ ($b_h^{1-DOF,tot} = 2D_h^{1-DOF,tot} \sqrt{k_h m_w}$) and $D_{\alpha}^{1-DOF,tot}$ ($b_{\alpha}^{1-DOF,tot} = 2D_{\alpha}^{1-DOF,tot} \sqrt{k_{\alpha} I_{\alpha}^E}$) of Wood et al. (2020) cannot be directly used for the parameterization of the structure. Indeed, since the experiments were not carried out in vacuum, these values include the structural damping, but also the damping induced by the surrounding air. The structure solver only requires the coefficients of the material damping in each degree of freedom. In order to determine these values, a series of 1-DOF free-oscillation simulations in still air is conducted for the vertical translation and the rotation around the y-axis. The numerical results are then compared with the experimental signals and the damping coefficients are systematically reduced until the decay of the motion

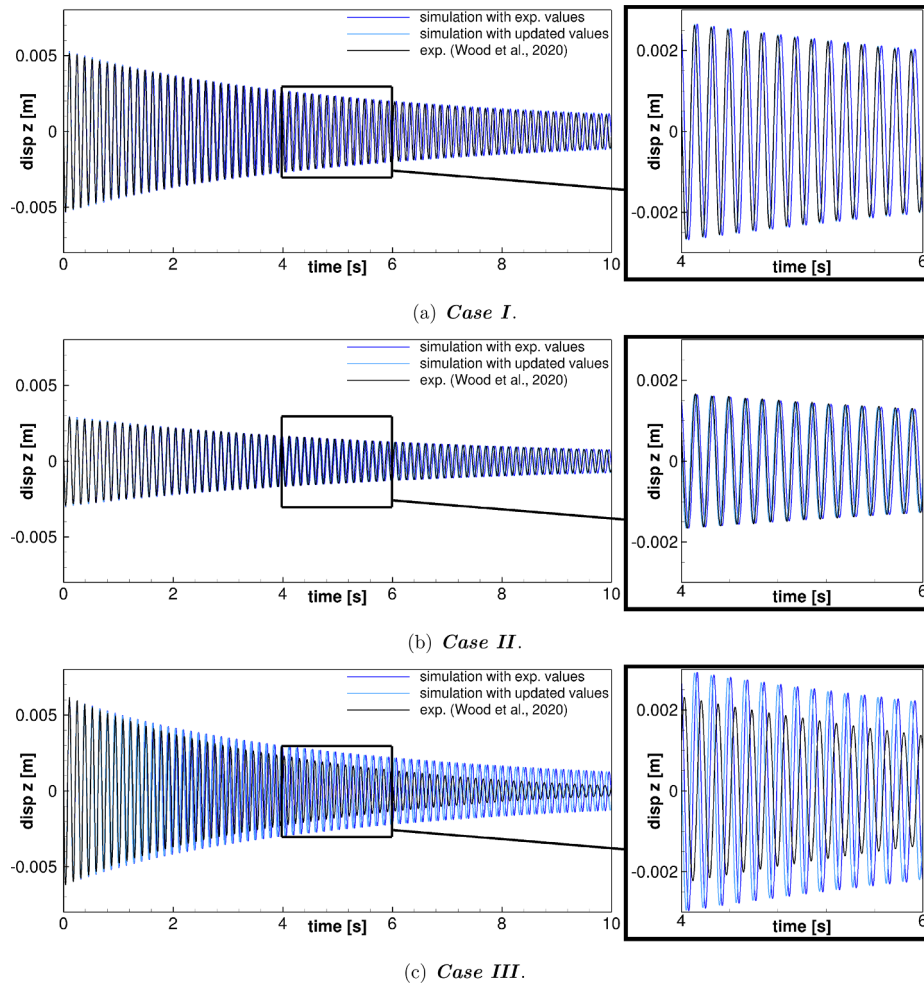


Fig. 4. Decay of motion (heave): Time evolution of the vertical displacement at the monitoring point P_w of numerical 1-DOF free-oscillation tests in still air compared with the experiments of Wood et al. (2020).

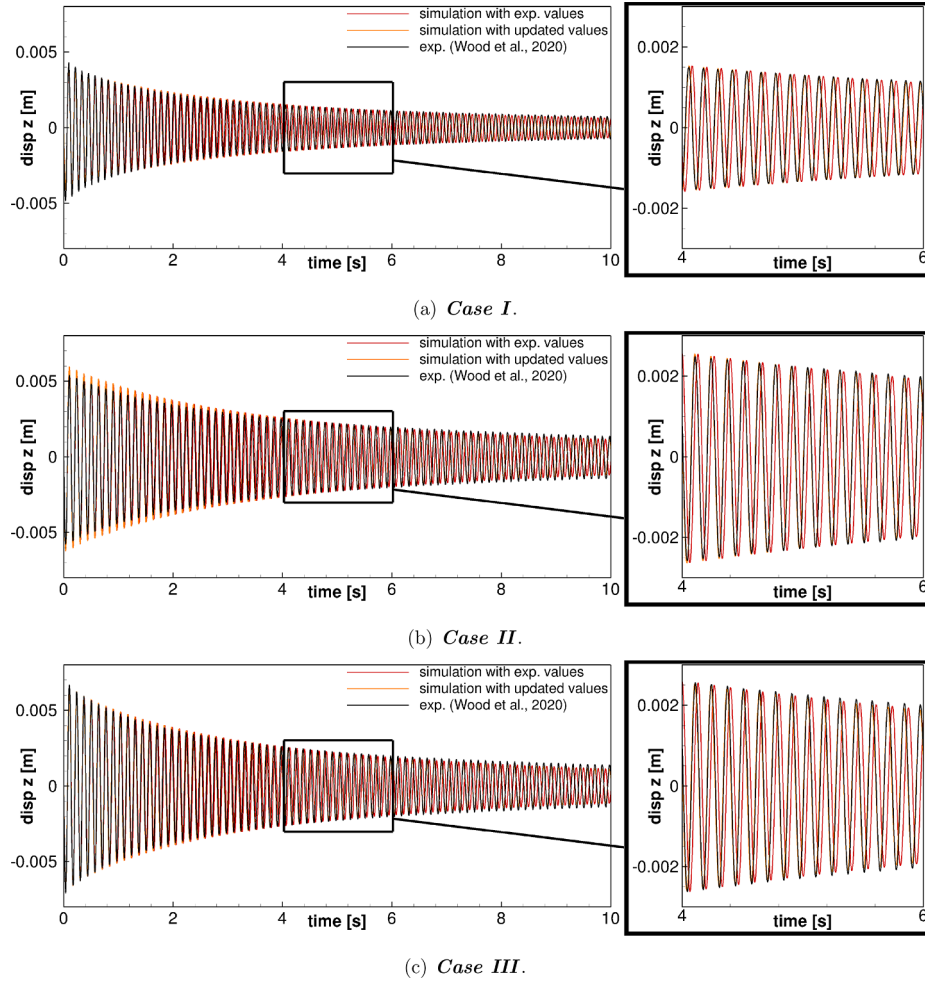


Fig. 5. Decay of motion (pitch): Time evolution of the vertical displacement at the monitoring point P_w of numerical 1-DOF free-oscillation tests in still air compared with the experiments of Wood et al. (2020).

Table 4
Predicted and measured heave and pitch frequencies with their relative error in case of the 1-DOF free-oscillation cases.

Parameter	Symbol	Unit	Case I	Case II	Case III
			$x_{EG} \approx 0$	$x_{EG} < 0$	$x_{EG} > 0$
Heave frequency	sim.	$f_h^{1-DOF, \text{sim, exp. values}}$	7.21	7.21	7.21
		$f_h^{1-DOF, \text{sim, updated values}}$	7.25	7.25	7.25
	exp.	$f_h^{1-DOF, \text{exp}}$	7.26	7.26	7.26
Relative error	ϵ_{f_h}	%	0.14	0.14	0.14
Pitch frequency	sim.	$f_\alpha^{1-DOF, \text{sim, exp. values}}$	8.28	7.45	7.45
		$f_\alpha^{1-DOF, \text{sim, updated values}}$	8.33	7.50	7.50
	exp.	$f_\alpha^{1-DOF, \text{exp}}$	8.33	7.49	7.49
Relative error	ϵ_{f_α}	%	0.00	0.13	0.13

Table 5
Updated main parameters.

Parameter	Symbol	Unit	Case I	Case II	Case III
			$x_{EG} \approx 0$	$x_{EG} < 0$	$x_{EG} > 0$
Distance between c.o.g. and e.a.	x_{EG}/c	-	0.006	-0.010	+0.059
Mass moment of inertia based on f_α^{1-DOF}	I_α^E	kg m ²	1.381×10^{-4}	1.708×10^{-4}	1.708×10^{-4}
Bending stiffness	k_h	N/m	705	705	705

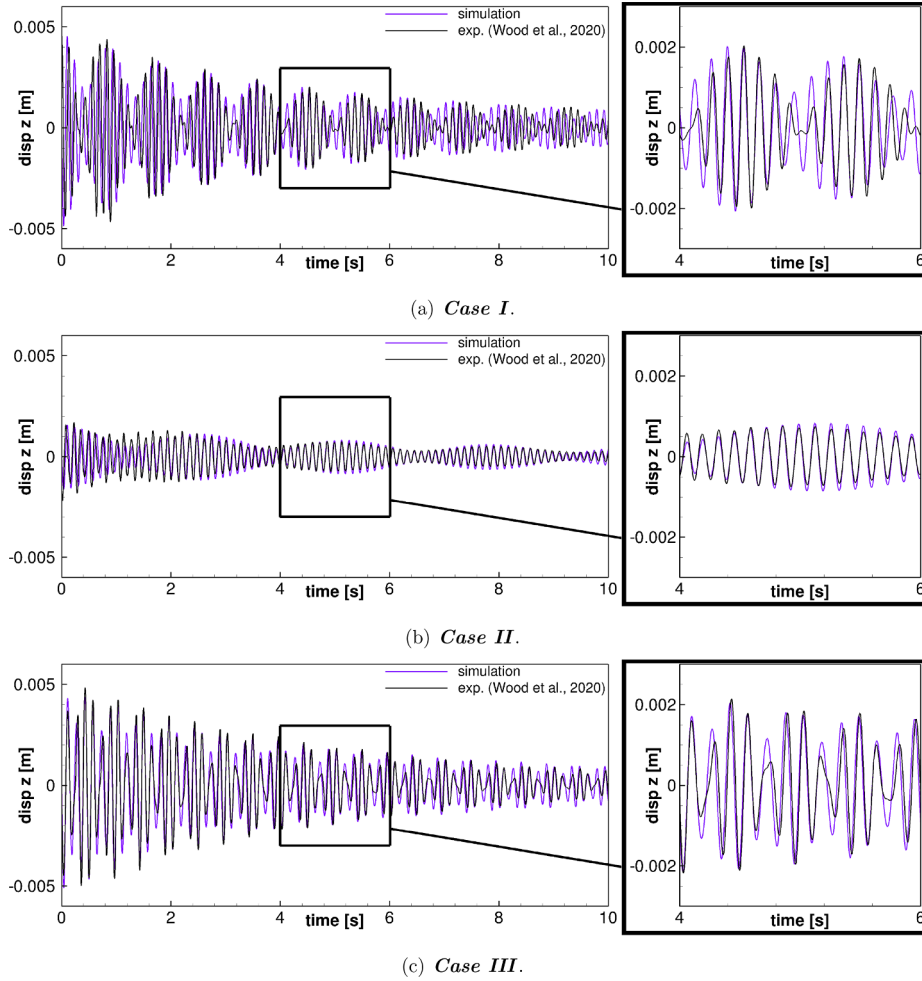


Fig. 6. Decay of motion of the coupled system: Time evolution of the vertical displacement at the monitoring point P_w of 2-DOF free-oscillation numerical tests in still air compared with the experiments of Wood et al. (2020).

Table 6

Initial vertical force F_z and moment M_y^E for the numerical 2-DOF free-oscillation tests in still air.

Parameter	Symbol	Unit	Case I	Case II	Case III
			$x_{EG} \approx 0$	$x_{EG} < 0$	$x_{EG} > 0$
Initial vertical force	F_z	N	-7.15×10^{-1}	-3.00×10^{-1}	-1.00×10^{-2}
Initial vertical moment	M_y^E	Nm	9.00×10^{-3}	1.00×10^{-3}	2.50×10^{-2}

coincides with the measurements. The outcome of this procedure is summarized in Table 3 providing the material damping ratios determined for the computational setup. Note that a unique set of damping ratios is chosen for cases I to III, since the spring system is the same for all three configurations (see explanations below). Moreover, the position of the center of gravity G does not play a role for these 1-DOF free-oscillation simulations. Therefore, the experimental values of x_{EG} are applied in these simulations.

In Figs. 4 and 5 the simulated vertical displacements of the monitoring point P_w of Wood et al. (2020) are compared with the experimental data for each case and each degree of freedom. The monitoring point P_w is located on the surface of the airfoil in a distance of $0.7c$ from the leading edge (see Fig. 1). In order to compute the vertical displacement at P_w , the heave z_E and the pitch angle α are combined by the following trigonometric relation $z_{P_w} = z_E + 2.8524 \times$

$10^{-2} \sin(0.1254 - \alpha)$. For these simulations the parameters determined by Wood et al. (2020) (see Table 2) and the newly determined material damping ratios summarized in Table 3 are used in a first step. Considering the decay of the displacement z_{P_w} of the heave and pitch, a quasi perfect fit is reached for case I and II with these parameters. In case III a close accordance is achieved for the pitch, but discrepancies are observed in the decay of the heave. A much stronger damping occurs in the experiment than in the simulation. This issue was already mentioned in Wood et al. (2020). While the total damping ratios of the pitch motions of the three cases were found to be similar with maximal deviations of about 10%, the values of the heave motion behave differently. For case I and II again comparable damping ratios were determined. However, for case III the total damping ratio of the heave motion was about two times larger than in the other two configurations. The first idea was to attribute the increase of the total damping ratio to an increased damping by the surrounding fluid. This possibility was investigated in the present simulations and could be excluded. Since the experiment (Wood et al., 2020) was reproducible and thus an error can be excluded, presently no final explanation can be provided. One option is that due to larger spring deformations in this case, some elastic dissipation occurs. Nevertheless, a unique set of damping ratios is applied in the simulations explaining the deviations observed.

Comparing the frequencies of the predicted displacements z_{P_w} with the experimental data, a good agreement is found in all cases for both DOF. However, small deviations still exist (see Table 4). The predicted heave frequency is slightly too low, whereas the opposite is true for the pitch frequency. To reduce this error, the bending stiffness k_h and the

Table 7
Predicted and measured heave and pitch frequencies with their relative errors in case of the 2-DOF free-oscillation cases.

Parameter		Symbol	Unit	Case I	Case II	Case III
				$x_{EG} \approx 0$	$x_{EG} < 0$	$x_{EG} > 0$
Heave frequency	sim.	$f_h^{2-DOF, \text{sim, updated values}}$	Hz	7.25	7.21	6.49
	exp.	$f_h^{2-DOF, \text{exp}}$		7.31	7.22	6.55
Relative error		ε_{f_h}	%	0.82	0.14	0.92
pitch frequency	sim.	$f_\alpha^{2-DOF, \text{sim, Updated values}}$	Hz	8.33	7.59	8.48
	exp.	$f_\alpha^{2-DOF, \text{exp}}$		8.38	7.53	8.51
Relative error		ε_{f_α}	%	0.60	0.80	0.35
Beat frequency	sim.	$f_{\text{beat}}^{2-DOF, \text{sim, updated values}}$	Hz	1.08	0.38	1.99
	exp.	$f_{\text{beat}}^{2-DOF, \text{exp}}$		1.07	0.31	1.96
Relative error		$\varepsilon_{f_{\text{beat}}}$	%	0.93	18	1.5

mass moment of inertia I_α^E are selected to be slightly adjusted. Indeed, in the system of equations describing the motion the experimental values of the mass m_w and the torsional stiffness k_α are considered to be exact, since the mass can be easily determined and the stiffness is provided by the manufacturer. Thus, the bending stiffness k_h and the mass moment of inertia I_α^E are obvious parameters to be adjusted to achieve a better match of the frequencies. The values are optimized to reduce the error below 0.5%. The corresponding values found by this procedure are summarized in Table 5. The bending stiffness k_α is marginally increased by about 1% and the mass moment of inertia I_α^E is decreased by about 1.3%. The vertical displacements at P_w predicted with this slightly adjusted set of parameters are also shown in Figs. 4 and 5 for each case. Obviously the agreement between the predicted results and the experimental data is further enhanced. Consequently, for both the validation study in Section 4.3 and the main results in Section 5 these improved parameters are applied.

4.3. Validation based on 2-DOF free-oscillation tests in still air

In order to validate the numerical setup, particularly the material damping coefficients evaluated in Section 4.2, a series of 2-DOF free-oscillation tests in still air is carried out for each case. As before, the predicted vertical displacements are compared with the experimental data at the same monitoring point P_w in Fig. 6. For each case the vertical displacement contains the superposition of the oscillation associated with the heave and the oscillation associated with the pitch. Since their frequencies f_h^{2-DOF} and f_α^{2-DOF} are not equal mathematically, the superposition of both quasi-periodic signals produces constructive and destructive interferences with a resulting frequency called the “beat frequency” $f_{\text{beat}}^{2-DOF} = |f_\alpha^{2-DOF} - f_h^{2-DOF}|$. Physically, an energy exchange between heave and pitch occurs in time. Contrary to the frequencies, the amplitude of these beats depends on the initial conditions. Since separated data of the initial heave and pitch are not available from the one-point measurements, a perfect fit regarding the beat amplitude is difficult to obtain. Note that for an initial excitation at the trailing edge in case II, the additional mass placed at the leading edge implies more initial heave than pitch. For a similar excitation the contrary is valid for case III. To generate the initial heave and pitch in the numerical 2-DOF free-oscillation tests in still air, a constant vertical force F_z and a constant moment M_y^E are applied during a short time interval of $\Delta T = 4 \times 10^{-3}$ s at the begin of the simulation. Afterwards, the system is left on its own. The values are summarized in Table 6.

The characteristic decay of motion and the associated beat frequency depend directly on the distance x_{EG} . Since this distance was roughly determined in the experiment (see Table 2), it needs to be adjusted by the try-and-error method to get a good fit with the

experimental signals.

First, case I with $x_{EG} \approx 0$ is discussed. Based on the material damping ratios (Table 3), the updated parameters in Table 5 and the initial conditions in Table 6, a good agreement between the predicted and the measured displacements is achieved as visible in Fig. 6a. A distance of $x_{EG}/c = 0.006$ is found to be an appropriate choice to describe the characteristic decay of motion of the 2-DOF simulation in still air. In order to determine the heave and pitch eigenfrequencies, power spectral densities (PSD) of the numerical results are evaluated and compared with the PSD of the experimental signal. The relative errors obtained on the heave, pitch and beat frequencies summarized in Table 7 are low and a very good agreement is achieved.

Note that additional simulations were carried out for the same setup but with only slightly different initial conditions for the heave and pitch in order to cope with the problem of the unknown initial conditions in the experiment. The results (not shown here) demonstrate that neither the envelope of the obtained signal nor the frequencies (heave, pitch and beat) change. However, the initial conditions obviously influence the positions of the maxima and minima within this envelope. That explains the deviations observed in Fig. 6a. Of course, the same uncertainty applies to the other two cases.

In case II the distance x_{EG} needs to be decreased in comparison with the experimental value to obtain an acceptable fit (see Table 5). Indeed for case II, both heave and pitch frequencies are close together, which implies a low beat frequency. Therefore, small errors of the eigenfrequencies lead to a large error of the beat frequency and to a visual mismatch of the decay of motion (see Fig. A16). To achieve a better fit for case II, the distance x_{EG} is reduced by 55% (from $x_{EG}/c = -0.022$ to -0.01). This shift appears large, but the displacement of G is in fact only 1.2 mm. Applying the updated x_{EG} and the updated values in Table 5, the predicted heave and pitch frequencies and the resulting beat frequency fit very well to the experimental data as shown in Table 7. Furthermore, the decay of motion is correctly simulated as visible in Fig. 6b.

Concerning case III no change in the experimentally determined value of x_{EG} is needed. In this case both heave and pitch frequencies are farther apart, resulting in a higher beat frequency, i.e., a fast transfer of modal energy between both DOF. With the updated values in Table 5 both simulated eigenfrequencies and the beat frequency match well with the measurements. An acceptable fit of the decay of motion is also found in Fig. 6c.

Since an overall good agreement for the decay of motion and for the heave and pitch frequencies on the 2-DOF test in still air is obtained for cases I, II and III, the computational setup is now validated. Thus, it can be used within the coupled simulations to investigate instantaneous phenomena such as flutter expected for certain free-stream velocities.

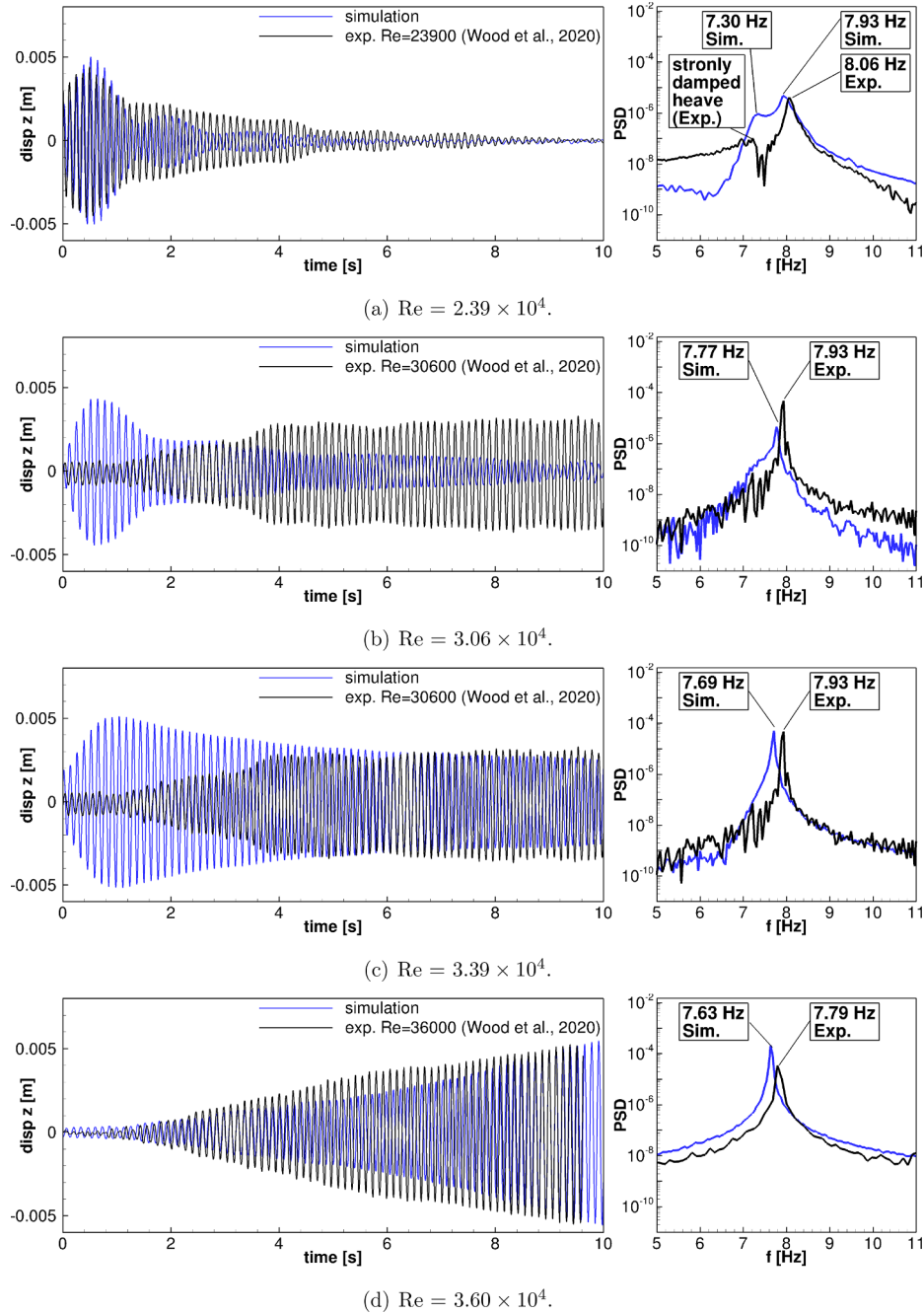


Fig. 7. Case I: Simulated motion of the coupled system: Time evolution of the vertical displacement at the monitoring point P_w of 2-DOF numerical tests in the Re range $2.39 \times 10^4 \leq Re \leq 3.60 \times 10^4$ compared with the experiments of Wood et al. (2020).

5. Results and discussion

After the validation study carried out for the 2-DOF free-oscillation tests in still air, the investigations of main interest are discussed in this section. Thus, the focus is now on the free-oscillation test case with 2-DOF under varying wind loads in the range between a damped characteristic up to the situation, where either limit-cycle oscillations or even flutter appear. For this purpose, the dynamic behavior of two configurations (*case I* and *III*) are taken into account. Since in the experiments (Wood et al., 2020) an increased flutter stability was found for *case II* and the free-stream velocity has to be more than doubled to end up with a LAO, this setup is not studied numerically. For the two other cases the results are analyzed and compared with the experimental data by Wood et al. (2020). The discussion starts with *case I* with

a quasi-zero static moment ($x_{EG} \approx 0$).

5.1. Case I: $x_{EG} \approx 0$

5.1.1. Small-amplitude oscillations

In the experiment (Wood et al., 2020) a very fast decay of the motion was observed after the initial excitation at the first two Reynolds numbers considered, i.e., $Re = 9.66 \times 10^3$ and 1.65×10^4 . Thus, they were interpreted as stable configurations without limit-cycle oscillations or flutter. Indeed, this is only half of the truth since marginally small oscillations with barely measurable amplitudes were found after the initial excitations have damped out. However, since the physical phenomenon responsible for these tiny oscillations (see explanations below) is exactly the same as for the case of $Re = 2.39 \times 10^4$,

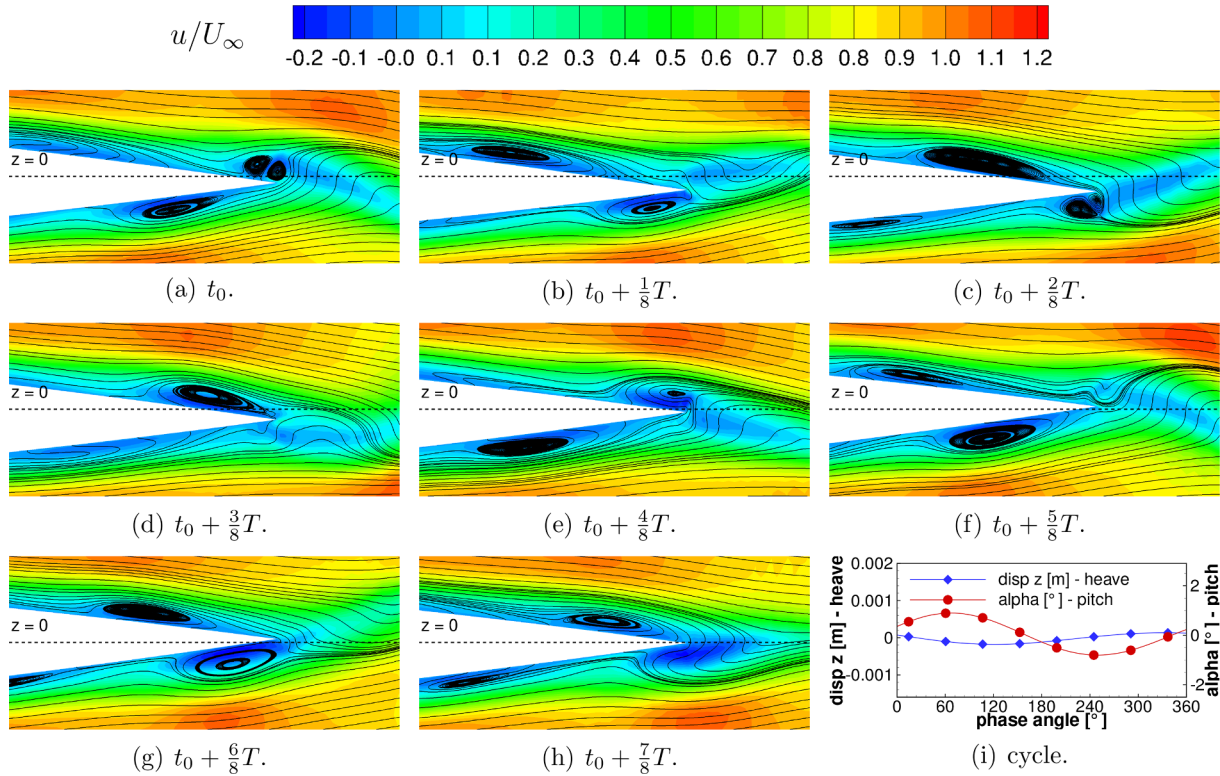


Fig. 8. Case I: One cycle of the airfoil oscillation (SAO) at $Re = 2.39 \times 10^4$ in the x - z -plane at $y = 0$ (close-up at the trailing edge with $x/c > 0.82$), streamwise velocity u normalized by the free-stream velocity U_∞ . The last diagram depicts the phase-shift angle between the heave and the pitch motion.

these two low Re numbers are not considered here. At $Re = 2.39 \times 10^4$ the situation is slightly different. Still a strongly damped heave motion is observed. The pitch motion is also severely damped. However, finally an oscillation amplitude remains which could be clearly measured and is denoted as small-amplitude oscillation (SAO) (amplitude below 0.2 mm). Note that in the simulations the observed amplitudes of the oscillations in case of $Re = 1.65 \times 10^4$ were found to be two orders of magnitude smaller than for $Re = 2.39 \times 10^4$.

Fig. 7a depicts the vertical displacement of the monitoring point P_v for the case of $Re = 2.39 \times 10^4$. Obviously, the initial excitation is damped very fast, but an oscillation with a very small but unmistakably ascertainable amplitude remains after the initialization phase. In Wood et al. (2020) it was speculated that the oscillations are caused by a laminar separation of the boundary layer which appears alternately on the upper and lower surface of the airfoil. However, based on the measurements it was not possible to prove this conjecture since the appearing recirculation regions are rather small. Of course, the predictions allow to clarify this issue. For this purpose, Fig. 8 depicts a series of snapshots of the flow field in the vicinity of the trailing edge. Based on the contour plots of the instantaneous streamwise velocity and the streamlines, the separated flow regions are visible appearing in an alternating manner on both sides of the airfoil. The pitch frequency is predicted at $f_h^{\text{sim}} = 7.93$ Hz and the frequency of the strongly damped heave at $f_\alpha^{\text{sim}} = 7.30$ Hz. Compared with the experimental value available for the pitch frequency a relative error of 1.6% is achieved. Similar to the measurements the heave is damped (see Fig. 8i). Since the heave and pitch frequencies are not equal, no phase-shift angle can be deduced. Fig. 9 provides a larger excerpt of the flow field by a series of eight snapshots representing a full cycle of the motion. Based on the streamwise velocity, the pressure coefficient and the vorticity component ω_y , it is obvious that solely in the vicinity of the trailing edge instantaneous phenomena in terms of flow separation and vortex generation take place.

5.1.2. Large-amplitude oscillations

As for the previous Reynolds number an initial perturbation is introduced for the simulation at $Re = 3.06 \times 10^4$ contrarily to the experiment. This measure is necessary since without any perturbation only a marginally small oscillation of the structure is observed. After a transition phase in which the amplitude of the initially disturbed motion decreases again, the airfoil continues to oscillate with a small amplitude below 0.4 mm (see Fig. 7b) and at a frequency of $f^{\text{sim}} = 7.77$ Hz. This amplitude is larger than for $Re = 2.39 \times 10^4$, but still rather small. Heave and pitch have the same frequency, which is predicted with a relative error of 1.7 % compared with the experiment. As for $Re = 2.39 \times 10^4$ the pitch dominates in terms of the amplitude. Although the predicted frequency is in close agreement with the experiment, the predicted motion behavior differs from the experimental one as visible in Fig. 7b. By slightly increasing the inflow velocity in the simulation up to $Re = 3.39 \times 10^4$ combined with the initial perturbation introduced before, the displacement of the airfoil after the initial phase fits to the experimental motion measured at $Re = 3.06 \times 10^4$. This is depicted in Fig. 7c. Indeed, a LAO with an amplitude of 0.003 m and a frequency of $f^{\text{sim}} = 7.69$ Hz is predicted with a phase-shift angle of $\varphi^{\text{sim}} = 138^\circ$, which also better fits to the experimental shift found at $Re = 3.06 \times 10^4$ ($\varphi^{\text{exp}} = 130^\circ$). As before the pitch motion is dominating over the heave (Fig. 10i).

Fig. 10 represents one complete cycle of the LAO of the airfoil. Contours of the streamwise velocity component u , the pressure coefficient c_p and the y -vorticity ω_y are depicted. During the whole cycle the flow is attached on both airfoil sides up about 2/3 of the chord length and vortices are continuously shed from the current suction side at a frequency of about 130 Hz corresponding to a Strouhal number ($St = f t_{\text{NACA}} / U_\infty$ with t_{NACA} is the thickness of the airfoil) of 0.31. As visible in the series of figures (Fig. 10), when the airfoil moves upwards the pitch angle is most of the time positive (and vice versa) generating more lift. In case of a limit-cycle oscillation this counteracts the damping of the heave motion.

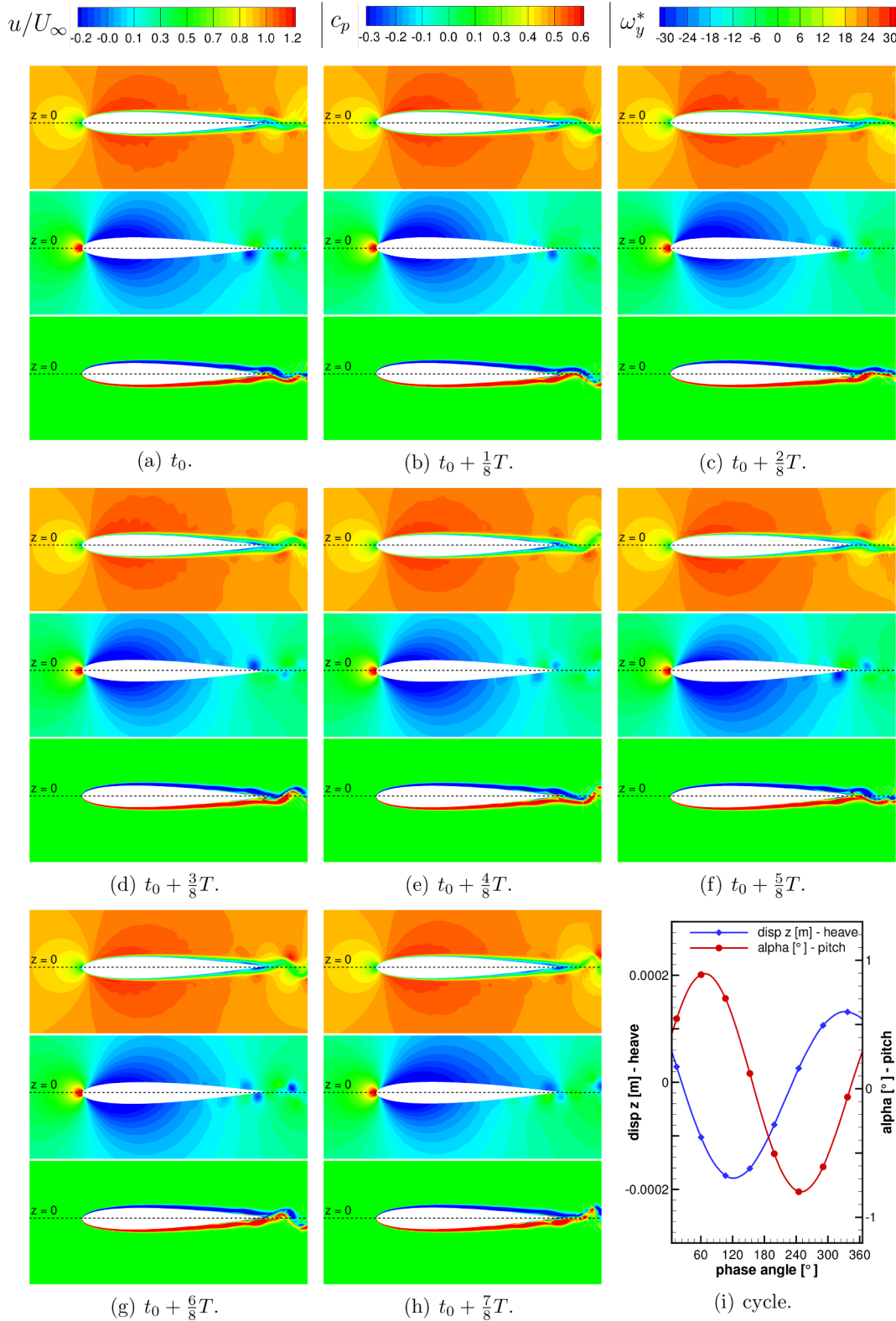


Fig. 9. Case I: One cycle of the airfoil oscillation (SAO) at $Re = 2.39 \times 10^4$ in the x - z -plane at $y = 0$, streamwise velocity u normalized by the free-stream velocity U_∞ (top), pressure coefficient c_p (middle), y -vorticity ω_y , normalized by the free-stream velocity U_∞ and the chord length c (bottom) (ω_y^*). The last diagram depicts the phase-shift angle between the heave and the pitch motion.

5.1.3. Flutter

At $Re = 3.60 \times 10^4$ the motion behavior changes: The amplitude of the displacement continuously increases without any initial perturbation as depicted in Fig. 7d. This fits to the observation made during the

experiment and can be denoted as flutter. In the experiment the motion of the airfoil was manually stopped to avoid the destruction of the springs. In the simulation the amplitude grows until the divergence of the coupled solver. Very large excitations of the airfoil with respect to

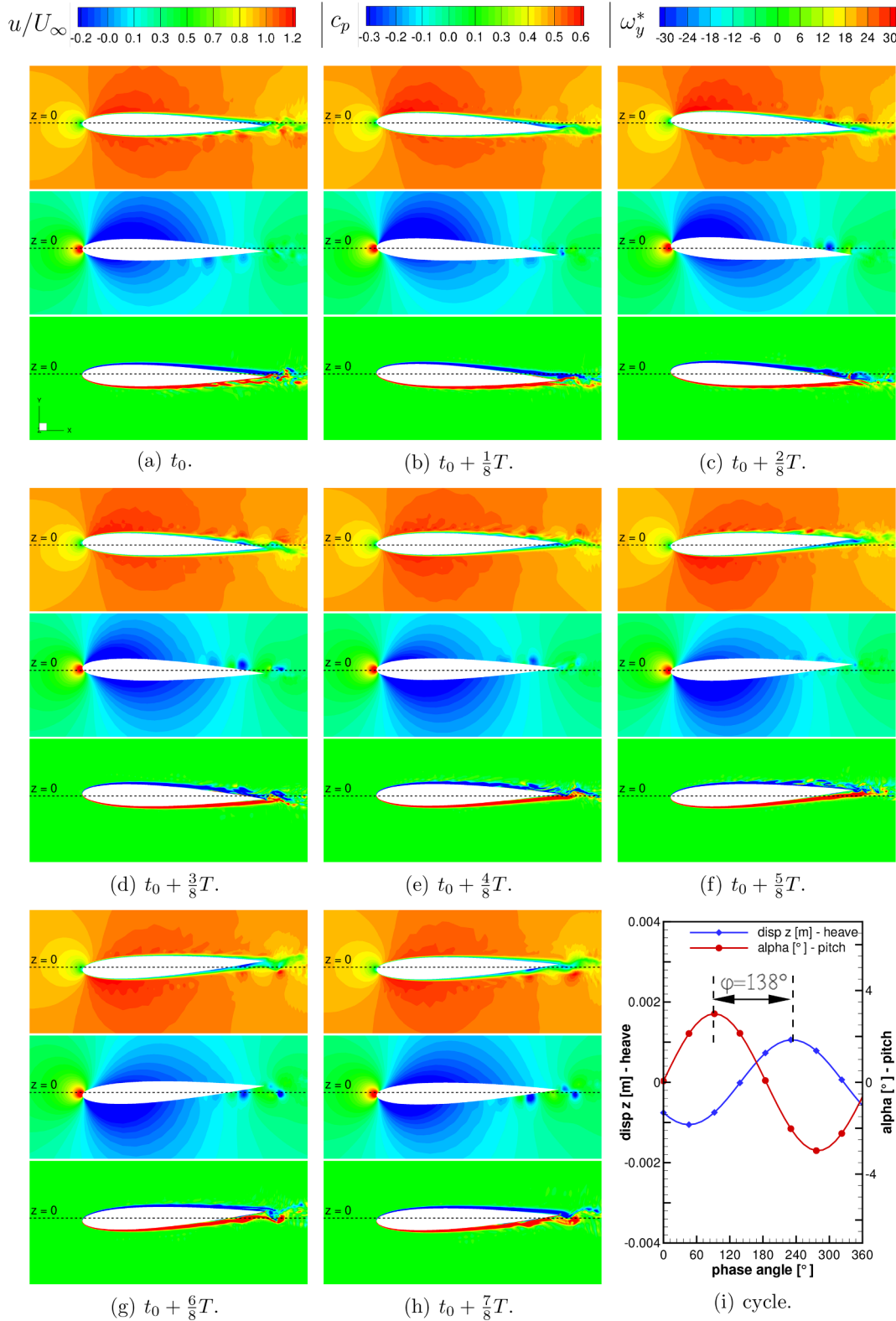


Fig. 10. Case I: One cycle of the airfoil oscillation (LAO) at $Re = 3.39 \times 10^4$ in the x - z -plane at $y = 0$, streamwise velocity u normalized by the free-stream velocity U_∞ (top), pressure coefficient c_p (middle), y -vorticity ω_y , normalized by the free-stream velocity U_∞ and the chord length c (bottom) (ω_y^*). The last diagram depicts the phase-shift angle between the heave and the pitch motion.

the heave and pitch motion lead to a strongly deformed grid and thus have to end up with a crash of the solver. Both heave and pitch occur at the same frequency, which is predicted at $f^{sim} = 7.63$ Hz. This flutter frequency is in close agreement with the experimental value

($f^{exp} = 7.79$ Hz). A phase-shift angle between pitch and heave of $\varphi^{sim} = 149^\circ$ is observed, which is slightly larger than the one measured by Wood et al. (2020) (see Table 8).

Fig. 11 represents one complete cycle of the airfoil motion at a given time ($t_0 \approx 20$ s), where the heave and pitch amplitudes (about 0.007 m

Table 8

Case I: Predicted and measured frequencies and phase-shift angle with their relative errors.

Case I	Symbol	Unit	SAO	LAO	Flutter	
			Heave (strongly damped)	Pitch		
Motion frequency	sim. f^{sim}	Hz	7.30	7.93	7.69	7.63
	exp. f^{exp}		Not available	8.06	7.93	7.79
relative error	ε_f	%	–	1.6	3.0	2.1
Phase-shift angle	sim. φ^{sim}	°	-	138	149	
	exp. φ^{exp}		-	130	137	
Relative error	ε_φ	%	-	6.2	8.8	

for the heave and about 12° for the pitch) are comparable with the maximal values provided in the experiments (about 0.005 m for the heave and about 12° for the pitch). As before, contours of the streamwise velocity component u , the pressure coefficient c_p and the y -vorticity ω_y are depicted. Starting at an instant in time, where the angle of attack is close to zero, the following observations can be made for the upper side of the airfoil. (Note that the lower side is not considered here since after the half of the period the phenomena observed on the upper side also appear on the lower side.) At the first snapshot depicted in Fig. 11a, a wholesome boundary layer exists along the entire chord length of the airfoil. Then the angle of attack increases leading to an adverse pressure gradient in Fig. 11b and to the appearance of flow separation close to the trailing edge. A vortical structure is generated visible by the low pressure region. With a further increase of the angle of attack depicted in Fig. 11c the separation moves upstream and additional low pressure regions are generated between $x/c = 0.5$ and 1.0 . A series of vortices is shed at the suction side at a frequency of about 145 Hz corresponding to a Strouhal number of 0.32, which is nearly identical to the St value observed at $Re = 3.39 \times 10^4$. When the angle of attack decreases again, the processes do not stop directly. Instead a hysteresis effect is observed. Thus, these phenomena are still visible in the next two snapshots of the series (i.e., Figs. 11d and 11e). The streamwise velocity even needs more time (see Fig. 11f and g) until all disturbances are gone and a wholesome boundary layer has developed again on the upper side (Fig. 11h). As mentioned above, identical observations can be made for the lower side at half a time interval later.

Similar to $Re = 3.39 \times 10^4$, when the airfoil moves upwards the pitch angle is most of the time positive (and vice versa) generating even more lift. However, for $Re = 3.60 \times 10^4$ this lift is stronger than the damping of the system amplifying the heave motion and contributing to the increase of the motion amplitude as expected in case of flutter.

It has to be noted that the motion behavior of the airfoil in case I highly depends on the distance x_{EG} . Indeed, for $x_{EG} = 0$ no flutter phenomenon is observed at $Re = 3.60 \times 10^4$, but an LAO. In that case flutter is achieved at about $Re = 4.69 \times 10^4$. That demonstrates the high sensitivity of this test case.

5.2. Case III: $x_{EG} > 0$

In case III the extra mass is mounted behind the elastic axis, thus $x_{EG} > 0$. x_{EG} is much larger than for case I and a value of $x_{EG}/c = 0.059$ was evaluated in Section 4.3. In the experimental study (Wood et al., 2020) a different behavior than for case I is observed for the free-oscillation test case with 2-DOF under varying wind loads. Up to $Re = 3.06 \times 10^4$ solely small-amplitude oscillations are found, where especially the heave motion experiences a very strong damping. Limited cycle oscillations with large amplitudes (LAO) are not detected at any Re number investigated. However, flutter sets in at $Re = 3.39 \times 10^4$ with a single characteristic frequency of 7.89 Hz and a much smaller phase-shift angle of $\varphi^{\text{exp}} = 25^\circ$ than for case I. This different behavior of

case III renders it an interesting case for the simulations.

At a Reynolds number of 4.1×10^4 this instability is also predicted by the simulation for case III with a frequency of $f^{\text{sim}} = 7.63$ Hz and a phase-shift angle between pitch and heave of $\varphi^{\text{sim}} = 25^\circ$. A relative error of only 3.3% on the predicted frequency and a full coincidence concerning the phase-shift angle are obtained. Thus, a good agreement with the experimental data is found. The pitch motion dominates over the heave motion in terms of amplitude: Angles larger than 20° are rapidly reached, whereas the heave motion oscillates below 4 mm.

Figs. 12 and 13 depict a complete cycle of the oscillation at an instant in time when the amplitudes are already large. The streamwise velocity normalized by the inflow velocity and the pressure coefficient are plotted in Fig. 12, whereas the y -vorticity ω_y , normalized by the free-stream velocity U_∞ and the chord length c and the instantaneous streamlines are shown in Fig. 13. The cycle starts with a nearly zero pitch angle (see Figs. 12a and 13a). The pitch angle grows extremely fast, while the heave motion increases more slowly. The large angle of attack leads to a massive separation of the flow and the formation of a large recirculation area directly at the leading edge on the suction side of the airfoil (see Figs. 12d and 13d). A clockwise rotating leading-edge vortex (LEV) forms, detaches and moves downstream during the decrease of the pitch angle (see Figs. 12e and 13e). Then, the flow reattaches again on the upper side due to the effect of the favorable pressure gradient. Due to the geometrical symmetry similar observations can be made half a period later for a negative pitch angle and a downward heave motion. At this instant in time the LEV representing a large quasi two-dimensional vortical structure is rotating in counter-clockwise direction. Since at this amplitude of motion two LEVs are shed during a cycle, the shedding frequency is about 15.2 Hz corresponding to a low Strouhal number of about 0.04. This shedding frequency and the frequency corresponding to the airfoil motion ($f^{\text{sim}} = 7.63$ Hz) are also clearly visible in the measured data for the wake (see Fig. 27 of Wood et al., 2020).

Contrarily to the experiment no physical limitations of the pitch angle and the heave motion are present in the simulations. Therefore, in case of the current instability found in the predictions, the pitch angle rapidly increases until the fluid solver diverges. At very large pitch angles the already described leading-edge vortex (LEV) and a second large vortical structure denoted trailing-edge vortex (TEV) form one after another and then combine to a complex rotating vortical structure convected downstream due to the free-stream velocity (see Figs. 14). Both LEV and TEV are quasi 2D structures at the Re numbers considered.

5.3. Comparison of the airfoil motions in case of dynamic instability

Sections 5.1 and 5.2 have presented the numerical results obtained for case I and III and compared them with the experimental data. In the current section the differences between both airfoil motions will be highlighted.

Fig. 15 schematically depicts the global motion of the airfoil in both cases. The airfoil simplified as a plate moves up and down following a sinusoidal curve representing the heave motion (in blue). At the same eight positions already shown in Figs. 11–13 the plate rotates by the pitch angle of the airfoil where the angles sketched in Fig. 15 are predicted by the simulations. Moreover, at each position two arrows denoting the direction of the heave motion (black arrow) and the direction of the lift force (red arrow) are added helping to understand the energy transfer during one cycle. In both cases the work generated by the lift is globally in the direction of the heave. Thus, when the energy due to the lift force is larger than the energy consumed by the structural damping, the amplitude of the motion increases.

In case I the heave motion contributes to the global motion of the airfoil with a comparable extent as the displacements generated by the pitch angle. Since the phase-shift angle is large, i.e., 149° , the maximum of the pitch angle is reached between the minimum and the zero

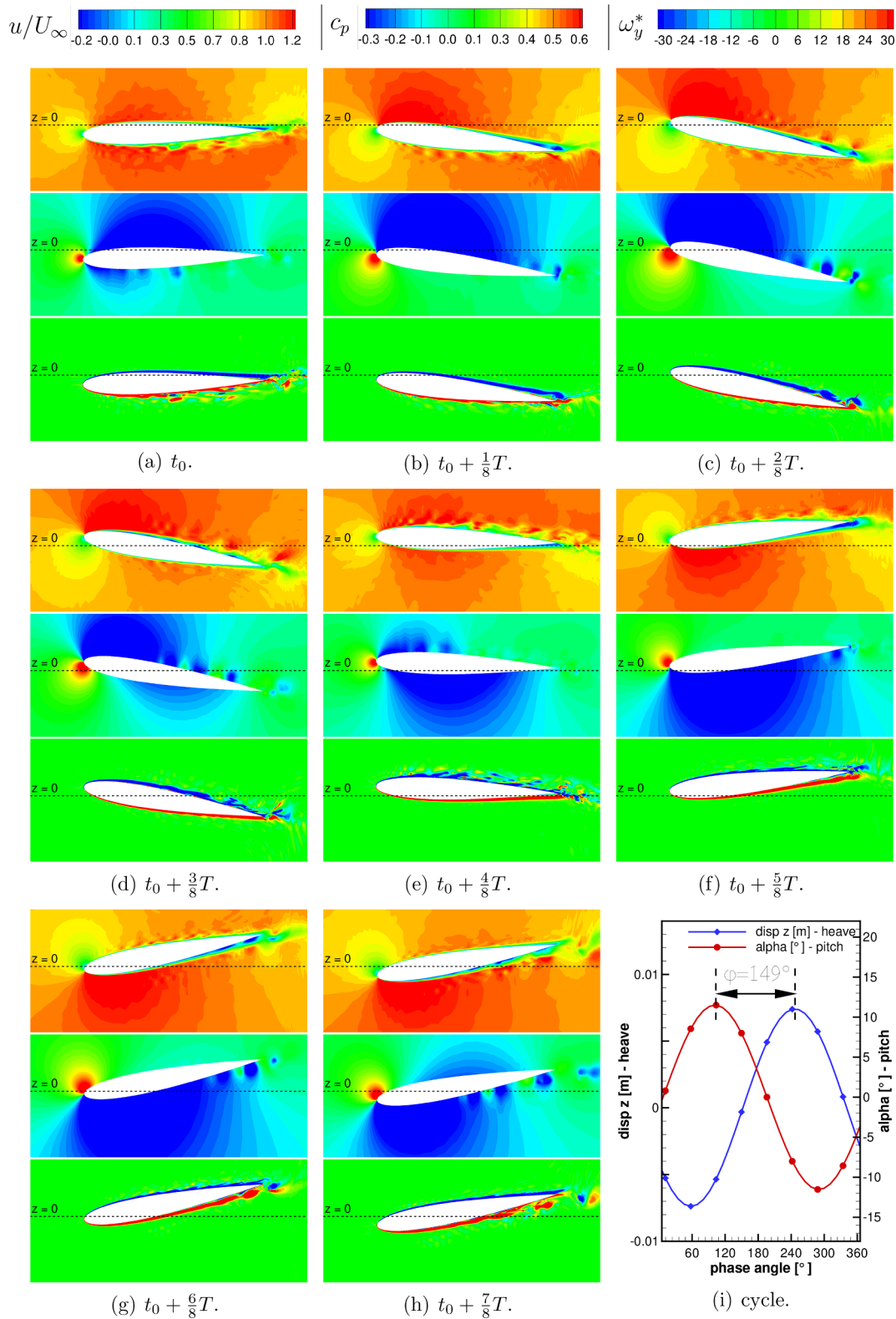


Fig. 11. Case I: One cycle of the airfoil oscillation (flutter) at $Re = 3.60 \times 10^4$ in the x - z -plane at $y = 0$, streamwise velocity u normalized by the free-stream velocity U_∞ (top), pressure coefficient c_p (middle) and y -vorticity ω_y normalized by the free-stream velocity U_∞ and the chord length c (bottom) (ω_y^*). The last diagram depicts the phase-shift angle between the heave and the pitch motion.

crossing of the heave motion (see Fig. 15a). That leads to a motion similar to a *swimming fish*.

In case III the contribution of the heave motion to the global motion is negligible compared to the pitching motion. The phase-shift angle is

much smaller, i.e., 25° leading to a maximum pitch angle just before the maximum of the heave motion is reached. Thus, the global motion of the airfoil looks like a *flapping wing*: The airfoil rotates around a virtual point located between the elastic axis and the trailing edge.

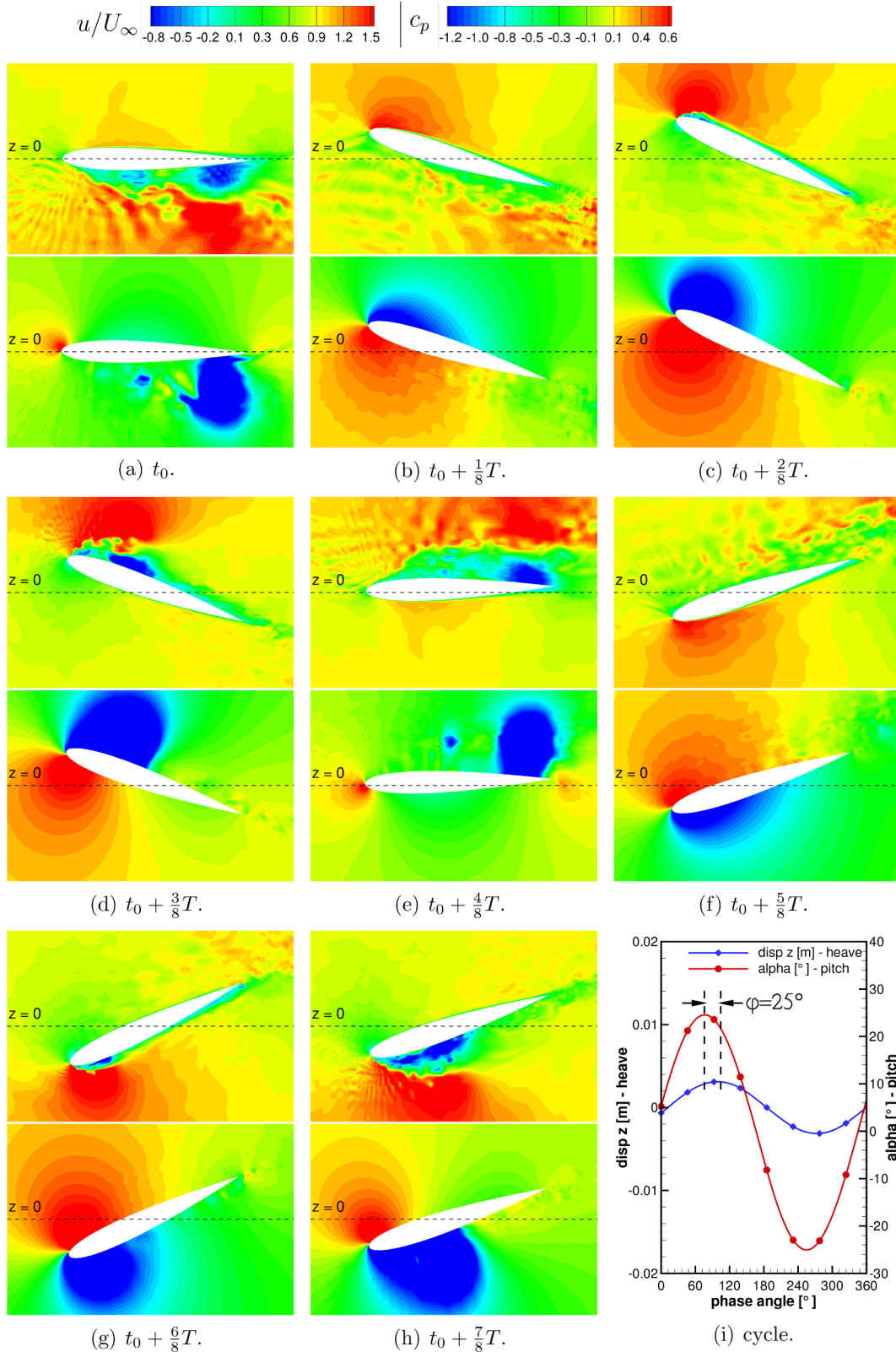


Fig. 12. Case III: One cycle of the airfoil oscillation (flutter) at $Re = 4.1 \times 10^4$ in the x - z -plane at $y = 0$, streamwise velocity u normalized by the free-stream velocity U_∞ (top) and pressure coefficient c_p (bottom). The last diagram depicts the phase-shift angle between the heave and the pitch motion.

6. Conclusions

Inspired by the experimental study (Wood et al., 2020), in which the dynamic behavior of an elastically mounted NACA 0012 airfoil with 2-DOF (heave and pitch) was investigated in the transitional Reynolds

number regime, the identical FSI setup was numerically studied in the present contribution. For this purpose, eddy-resolving simulations of the fluid flow were coupled with a solver for describing the translation and rotation of the wing within a partitioned coupling scheme. In a first step the material parameters provided by the measurements were

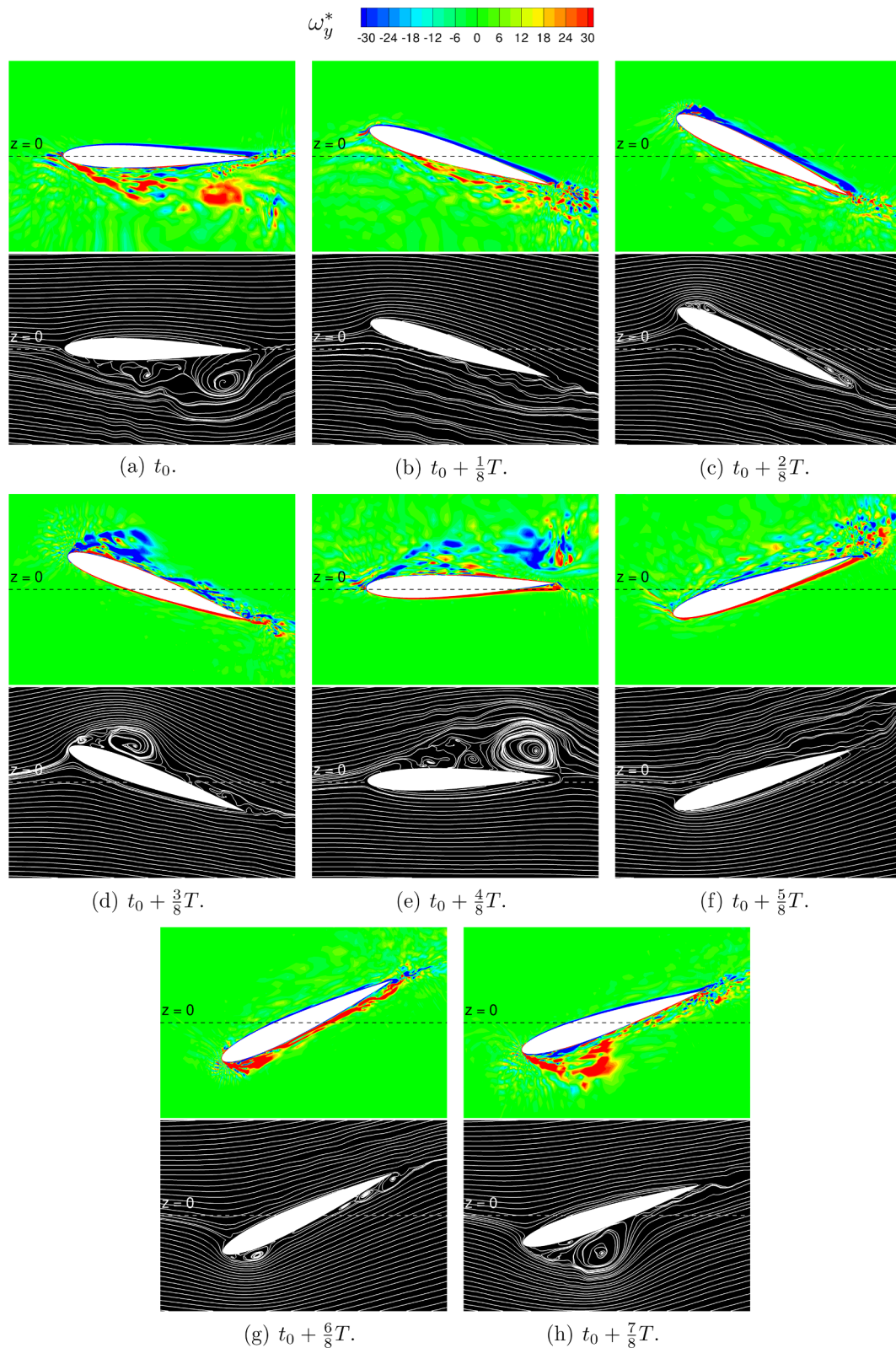


Fig. 13. Case III: One cycle of the airfoil oscillation (flutter) at $Re = 4.1 \times 10^4$ in the x - z -plane at $y = 0$, y -vorticity ω_y , normalized by the free-stream velocity U_∞ and the chord length c (bottom) (ω_y^*) and instantaneous streamlines (bottom).

proven and the missing pure material damping coefficients were determined based on 1-DOF free-oscillation tests in still air. A subsequent validation step was carried out exploiting the corresponding 2-DOF free-oscillation tests in still air. After these important steps the actual investigations considered two cases (center of gravity nearly identical

to the elastic axis (*I*) and behind (*III*) the e.a.) of the wing under various free-stream velocities. The main findings of the study are:

- The coupled high-fidelity solver allows to predict the FSI problem with an acceptable accuracy leading to either small/large-amplitude

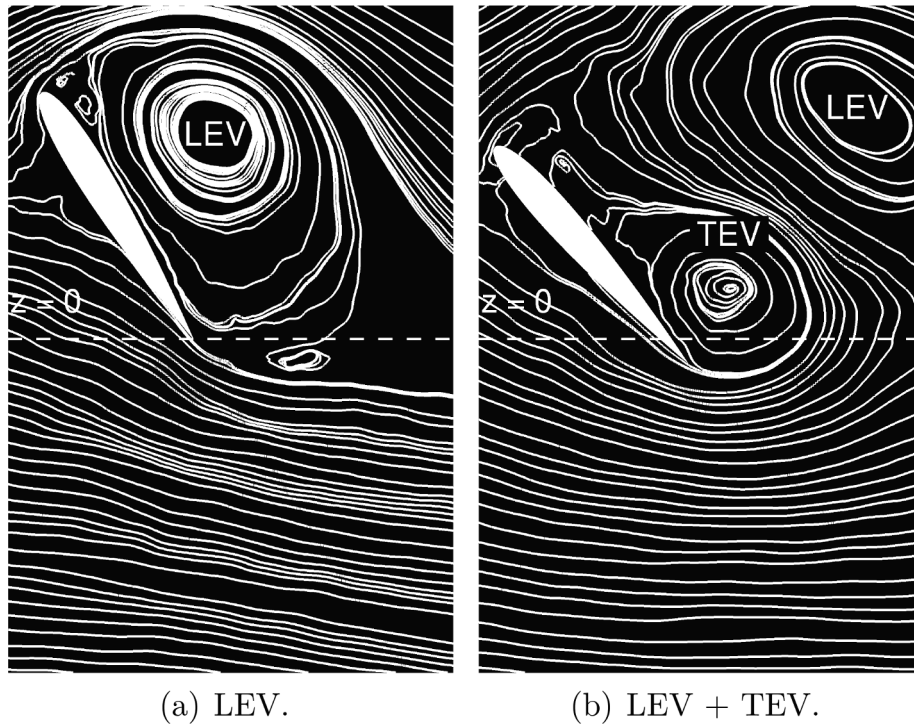


Fig. 14. *Case III*: Formation and shedding of leading-edge vortex (LEV) and trailing-edge vortex (TEV) at very large angles of attack.

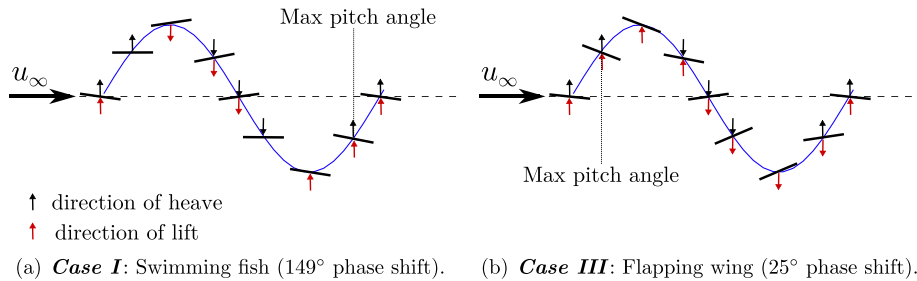


Fig. 15. Comparison of the airfoil motion.

oscillations or flutter depending on the case and Re number considered.

- Nevertheless, a very high sensitivity of the 2-DOF coupled case is observed. That comprises on the one hand side the governing properties of the setup such as the mass moment of inertia, the stiffness and the damping ratio. On the other hand the geometrical distance between the center of gravity and the elastic axis is found to be a very decisive parameter, which has to be determined very carefully, in order to lay the basic premise that measurements and predictions can match.
- Especially *case I*, where the center of gravity approximately coincides with the elastic axis, was studied in detail by successively increasing the Reynolds number. At the two lowest Re numbers considered limit-cycle oscillations with marginally small and thus barely measurable amplitudes are observed in the predictions in agreement with the measurements. First small-amplitude oscillations with unmistakably ascertainable displacements are detected at $Re = 2.39 \times 10^4$ which are dominated by a pitch motion, whereas the heave motion is strongly damped. Large-amplitude oscillations are measured in the experiment at $Re = 3.06 \times 10^4$. However, at this Re number the predicted amplitudes are still rather small. An increase of the Re number by about 10% significantly changes the situation. Now, the predicted amplitudes are in close agreement

with the experimentally measured LAO. Finally, at $Re = 3.60 \times 10^4$ flutter is found for both, the measurements and the predictions. The flutter frequency and the shift in the phase angle between pitch and heave are in reasonable agreement. Contrary to the experiments the simulations allow to study the entire flow phenomena appearing during a complete cycle of the airfoil oscillation, which is governed by a series of vortices and flow separation appearing close to the trailing edge.

- When increasing the distance x_{EG} between the center of gravity and the elastic axis (i.e., *case III*), the dynamic system reveals a stronger coupling between the heave and the pitch motion associated with a significantly smaller phase-shift angle than in *case I*. In agreement with the experiment (Wood et al., 2020) a phase-shift angle of $\varphi = 25^\circ$ is found for *case III*. Thus, the associated motion patterns of both cases significantly deviate. The motion in *case I* is comparable to a swimming fish, whereas the movement pattern in *case III* can be described by a flapping wing. Both scenarios are well reproduced in the predictions.
- Furthermore, the flow field in *case III* observed during the flutter scenario is dominated by large-scale vortical structures arising at the leading-edge (LEV) and for even large angles of attack also at the trailing edge (TEV). These flow phenomena can be adequately predicted by the applied large-eddy simulation technique.

Declaration of Competing Interest

The authors declare that they have no known competing financial interests or personal relationships that could have appeared to influence the work reported in this paper.

Acknowledgments

The authors want to thank Larissa Streher (University of Groningen,

The Netherlands) and Benjamin Künzel (University of German Armed Forces Hamburg, Germany) who did pre-studies for this work during their master thesis and also Alban Leroyer (Ecole Centrale Nantes, France) for the interesting exchange on the quaternions and Newton's second law.

Appendix A. Case II: 2-DOF free-oscillation test in still air applying the experimentally determined value of $x_{EG}/c = -0.022$

Fig. A16

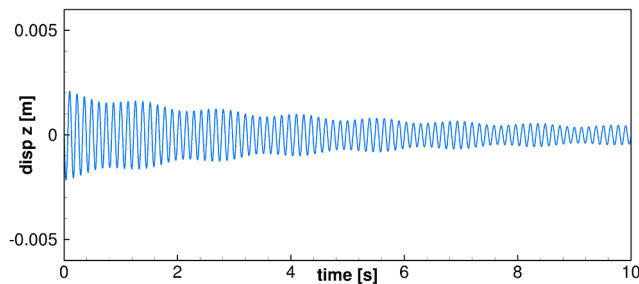


Fig. A16. Case II: Predicted time evolution of the vertical displacement at the monitoring point P_w of 2-DOF free-oscillation tests in still air applying the experimentally determined value of $x_{EG}/c = -0.022$.

Appendix B. Supplementary data

Supplementary data associated with this article can be found, in the online version, at <https://doi.org/10.1016/j.ijheatfluidflow.2020.108631>.

References

- Almutari, J.H., 2011. Large-eddy simulation of flow around an airfoil at low Reynolds number near stall. Ph.D. thesis, University of Southampton, England, available online: http://eprints.soton.ac.uk/181533/1.hasCoversheetVersion/Jaber_Thesis.pdf.
- Apostolatos, A., De Nayer, G., Bletzinger, K.-U., Breuer, M., Wüchner, R., 2019. Systematic evaluation of the interface description for fluid-structure interaction simulations using the isogeometric mortar-based mapping. *J. Fluids Struct.* 86, 368–399.
- Breuer, M., 2002. Direkte Numerische Simulation und Large-Eddy Simulation turbulenter Strömungen auf Hochleistungsrechnern. Habilitationsschrift, Universität Erlangen-Nürnberg, Berichte aus der Strömungstechnik. Shaker Verlag, Aachen, Germany.
- Breuer, M., 2018. Effect of inflow turbulence on an airfoil flow with laminar separation bubble: An LES study. *Flow Turbul. Combust.* 101 (2), 433–456.
- Breuer, M., De Nayer, G., Münsch, M., Gallinger, T., Wüchner, R., 2012. Fluid-structure interaction using a partitioned semi-implicit predictor-corrector coupling scheme for the application of large-eddy simulation. *J. Fluids Struct.* 29, 107–130.
- Causin, P., Gerbeau, J.F., Nobile, F., 2005. Added-mass effect in the design of partitioned algorithms for fluid-structure problems. *Comput. Methods Appl. Mech. Eng.* 194, 4506–4527.
- De Nayer, G., Apostolatos, A., Wood, J.N., Bletzinger, K.-U., Wüchner, R., Breuer, M., 2018. Numerical studies on the instantaneous fluid-structure interaction of an air-inflated flexible membrane in turbulent flow. *J. Fluids Struct.* 82, 577–609.
- De Nayer, G., Breuer, M., 2014. Numerical FSI investigation based on LES: flow past a cylinder with a flexible splitter plate involving large deformations (FSI-PfS-2a). *Int. J. Heat Fluid Flow* 50, 300–315.
- De Nayer, G., Kalmbach, A., Breuer, M., Sicklinger, S., Wüchner, R., 2014. Flow past a cylinder with a flexible splitter plate: a complementary experimental-numerical investigation and a new FSI test case (FSI-PfS-1a). *Comput. Fluids* 99, 18–43.
- De Nayer, G., Schmidt, S., Wood, J.N., Breuer, M., 2018. Enhanced injection method for synthetically generated turbulence within the flow domain of eddy-resolving simulations. *Comput. Math. Appl.* 75 (7), 2338–2355.
- Durst, F., Schäfer, M., 1996. A parallel block-structured multigrid method for the prediction of incompressible flows. *Int. J. Numer. Methods Fluids* 22 (6), 549–565.
- Farhat, C., van der Zee, K.G., Geuzaine, P., 2006. Provably second-order time-accurate loosely-coupled solution algorithms for transient non-linear computational aeroelasticity. *Comput. Methods Appl. Mech. Eng.* 195 (17–18), 1973–2001.
- Fung, Y.C., 2008. An Introduction to the Theory of Aeroelasticity, third ed. Courier Dover Publications.
- Germano, M., Piomelli, U., Moin, P., Cabot, W.H., 1991. A dynamic subgrid-scale eddy viscosity model. *Phys. Fluids A* 3, 1760–1765.
- Kalmbach, A., Breuer, M., 2013. Experimental PIV/V3V measurements of vortex-induced fluid-structure interaction in turbulent flow—A new benchmark FSI-PfS-2a. *J. Fluids Struct.* 42, 369–387.
- Knupp, P.M., 2003. Algebraic mesh quality metrics for unstructured initial meshes. *Finite Elem. Anal. Des.* 39 (3), 217–241.
- Leroyer, A., Visonneau, M., 2005. Numerical methods for RANSE simulations of a self-propelled fish-like body. *J. Fluids Struct.* 20 (7), 975–991.
- Lian, Y., Shyy, W., Viieru, D., Zhang, B., 2003. Membrane wing aerodynamics for micro air vehicles. *Prog. Aerosp. Sci.* 39 (67), 425–465.
- Lilly, D.K., 1992. A proposed modification of the Germano subgrid-scale closure method. *Phys. Fluids A* 4, 633–635.
- Mueller, T.J., 2001. An overview of micro air vehicle aerodynamics. In: Mueller, T.J. (Ed.), Fixed and Flapping Wing Aerodynamics for Micro Air Vehicle Applications. Vol. 195 of Progress in Aeronautics and Astronautics. American Institute of Aeronautics and Astronautics Inc, pp. 1–10.
- Newmark, N.M., 1959. A method of computation for structural dynamics. *J. Eng. Mech. Div.* 85 (3), 67–94.
- Sen, S., De Nayer, G., Breuer, M., 2017. A fast and robust hybrid method for block-structured mesh deformation with emphasis on FSI-LES applications. *Int. J. Numer. Methods Eng.* 111 (3), 273–300.
- Shyy, W., Berg, M., Ljungqvist, D., 1999. Flapping and flexible wings for biological and micro air vehicles. *Prog. Aerosp. Sci.* 35 (5), 455–505.
- Smagorinsky, J., 1963. General circulation experiments with the primitive equations I: the basic experiment. *Mon. Weather Rev.* 91 (3), 99–165.
- Wood, J.N., Breuer, M., De Nayer, G., 2020. Experimental investigations on the dynamic behavior of a 2-DOF airfoil in the transitional Re number regime based on digital-image correlation measurements. *J. Fluids Struct.* 96, 103052.
- Wood, J.N., De Nayer, G., Schmidt, S., Breuer, M., 2016. Experimental investigation and large-eddy simulation of the turbulent flow past a smooth and rigid hemisphere. *Flow Turbul. Combust.* 97 (1), 79–119.